Self-organized fingering instabilities drive the emergence of tissue morphogenesis in digit organoids.

Rio Tsutsumi[1,2*], Antoine N. Diez[1,3], Steffen Plunder[1], Ryuichi Kimura[4,5], Shinya, Oki[4,5], Kaori Takizawa[2], Haruhiko Akiyama[6, 7], Yusuke Mii[2,8], Ritsuko Takada[8], Shinji Takada[8], Mototsugu Eiraku[2*]

[1]Institute for Advanced Study of Human Biology (WPI-ASHBi), Kyoto University, Kyoto, 606-8303, Japan

[2]Institute for Life and Medical Sciences (LiMe), Kyoto University, Kyoto, 606-8507, Japan

[3]Mathematical Application Research Team, Division of Applied Mathematical Science, RIKEN Center for Interdisciplinary Theoretical and Mathematical Sciences (iTHEMS), RIKEN iTHEMS Wako, Saitama 351-0198, Japan

[4]Department of Drug Discovery Medicine, Kyoto University Graduate School of Medicine, Kyoto, 606-8507, Japan

[5]Institute of Resource Development and Analysis, Kumamoto University, Kumamoto, 860-0811, Japan

[6]Department of Orthopaedic Surgery, Graduate School of Medicine, Gifu University, Gifu, 501-1194, Japan

[7]Center for One Medicine Innovative Translational Research (COMIT), Institute for Advanced Study, Gifu University, Gifu, 501-1193, Japan

[8]National Institute for Basic Biology and Exploratory Research Center on Life and Living Systems (ExCELLS), National Institutes of Natural Sciences, Aichi, 444-8787, Japan

*Correspondence should be addressed to R.T. (tsutsumi.rio.8x@kyoto-u.ac.jp) and M.E. (eiraku.mototsugu.2u@kyoto-u.ac.jp).

Abstract

Tissue morphogenesis is an emergent phenomenon: macroscopic structures cannot be predicted from a parts list of genes and cells. We examined how digits arise from a spherical limb bud and present a framework linking microscopic behaviors to morphogenesis. To extract digit morphogenesis *in vitro*, we created a limb-mesenchyme organoid that breaks symmetry and forms digit-like cartilage. Analyzing cell behaviors and iterating with cellular-based models identified sufficient microscopic mechanisms: differential adhesion between Distal and Proximal cells, chemotaxis toward Fgf8b and Wnt3a, and biased traction driving convergent extension. Taking the continuum limit of these behaviors yielded a modified Cahn–Hilliard equation that can describe fingering instability, recapitulating organoid morphogenesis. Taken together, this work suggests that the emergence of "fingers" can be explained as fingering instability.

Introduction

The last few decades of developmental biology have yielded an extraordinary map of the molecular landscape underlying embryonic development. In many systems, including limb development, we now know the genes that serve as **morphogenetic "keys"**—those whose activation unlocks the entire morphological programs, such as Hox and Tbx4, 5 (*1–4*). We also know the molecular and cellular **"ingredients"** of these programs: the structural proteins, the signaling molecules that mediate cell-cell communication, and the cellular behaviors such as chemotaxis or convergent extension that physically drive tissue shaping. This reductionist framework has been successful in identifying the necessary components of development. Yet, knowing the necessary components is still insufficient to explain how almost the same set of cell types gives rise to different structures, such as hands, feet, jaws, and even a formless teratoma. In other words, despite having the list of necessary components, we remain unable to answer a simple, fundamental question: **How does a tissue acquire its specific shape?** This reflects an emergent nature of tissue morphogenesis; its macroscopic patterns and structures cannot be readily predicted by listing its molecular and cellular parts (*5*).

To address this problem, we sought to apply the principles of statistical physics, where the collective behavior of many interacting components gives rise to emergent macroscopic properties. Applying this framework to biology requires describing the behaviors of cells and molecules mathematically and considering the limit of large numbers, thereby bridging microscopic behaviors and tissue-scale morphogenesis. Importantly, it also requires experimental systems where the complexity of embryonic development can be distilled into simplified, controllable conditions (*6*). Multicellular *in vitro* models such as micropatterning cultures, micromass cultures, and organoids provide such a platform. In these systems, we can observe self-organization—the spontaneous emergence of multicellular patterns from minimal initial conditions (*7–10*). In dynamical systems theory, such self-organization is often attributed to instabilities, where small perturbations are amplified to produce macroscopic structure. Therefore, if we can mathematically account for instability, we would essentially explain the mechanism of self-organization and, by extension, the emergence of tissue morphogenesis. For this purpose, we aim to build simple organoid systems extracting essential biophysical rules amenable to mathematical analysis, rather than recapitulating *in vivo* complexity (*11*).

In biology, a widely cited theory in this role is Turing instability, exemplified by the models to explain digit cartilage patterning (*12*, *13*). Those studies are inspired by the spontaneous formation of stripes-and-dots patterns in high-density micromass culture and, by extension, successfully explained cartilage patterning of the developmental limb bud using the same frameworks. However, Turing instability, by definition, arises from molecular reaction-diffusion processes, whose diffusion itself is often not directly observable. Thus, we set out to reinterpret digit morphogenesis using a model grounded in directly observable cellular and molecular migration. By combining a novel *in vitro* limb organoid model with mathematical analysis based on the agent (cellular)-based models (ABM) and derivation of the partial differential equations (PDE), we reveal an alternative instability mechanism driving the emergence of tissue-level morphogenesis.

Results

Fgf8 and Wnt3a sufficiently induces morphogenesis of digit-like structures from limb mesenchymal cells in vitro

It has been shown that Fgf8b and Wnt3a (FW), which are the main signaling factors secreted from the apical ectodermal ridge (AER), modulate the timing and patterns of cartilage differentiation in the micromass culture (*14–16*), and Turing models have interpreted these observations as the modulated wavelength by Fgf signaling (*12*, *17*). While Turing models do not require a cellular subpopulation with a specific potential to organize cartilage patterns, the other studies suggested that the Distal-Proximal cellular heterogeneity governs the differences in self-organizing potential of distal cartilage (*18*, *19*). To integrate the involvement of signaling molecules such as FW and cellular heterogeneity, we performed the micromass culture after labeling the limb mesenchymal cells derived from the Distal (digits) and the Proximal (palm) part of the autopods in the Sox9-GFP (to visualize the cartilage differentiation) mouse embryos at E11.5, as H2BtdTomato and H2BtagBFP. Our live imaging on the micromass culture showed that the supplementation of FW to the medium (FW condition) seemed to promote the cell sorting between the Distal and Proximal cells and the Distal cell clusters exhibited the stronger signal of Sox9-GFP than the Proximal cells or unclustered Distal cells, while the differences are not seen in the serum only condition (negative control: NC) (Fig. 1 A, B, Supplementary movie 1). Quantitatively, the Distal cells with more than nine Distal cells among their 10 neighbors increased, and those cells exhibited higher Sox9-GFP intensities (Fig. 1B, C). To quantify the cell sorting, we computed the nearest

neighbor score (NNS) by counting the number of the same type of cells (Distal or Proximal) and normalizing it such that the score would be one under the null hypothesis (random distribution), while the score would be higher when cell sorting occurs (See methods). The results showed that the cell sorting was promoted in FW condition (Fig. 1D).

To further assess the involvement of FW condition in cartilage morphogenesis *in vitro*, we cultured 9,000 cells of the limb mesenchyme derived from Sox9-GFP mouse embryos as a cellular aggregate in a three-dimensional environment. The result showed that while the aggregates cultured in NC condition maintained their spherical shapes, the ones cultured in FW condition broke their symmetry and exhibited the elongation of stick-shaped cartilage despite the fact that we did not introduce any directionality of the FW signals (Fig. 1E, Supplementary movie 2). Interestingly, when the starting number of the cells was increased to 27,000 cells in FW condition, the aggregate produced multiple bifurcated cartilage rather than the isotropic scaling up (Fig. 1E, S1). Consistently with the micromass culture, when Distal and Proximal cells were labeled by H2BVenus and H2BtdTomato, respectively, while Distal and Proximal cells were intermingled in NC condition, Distal and Proximal cells were sorted out each other in FW condition within 24 hours, subsequently the Distal cluster elongated. Thus, the symmetry was broken through the cell sorting between Distal and Proximal cells (Fig. 1F, Supplementary movie 3). Notably, when the starting number was increased to 27,000 cells in FW condition, the Distal cells tended to cluster at multiple places, explaining the mechanism of the bifurcation of the cartilage. Thus, FW sufficiently induced the symmetry breaking of the cellular aggregate and elongation of the cartilage without directionality of the signals (Fig. 1G). Interestingly, we could also observe the separation of the cartilage in the middle, reminiscent of joint formation (Fig. 1G).

The spatial transcriptomics experiments by UV-induced local *in vitro* reverse transcriptions called photo-isolation chemistry (PIC) (*20*) showed that genes highly expressed in the tip of the aggregate corresponded to the genes expressed in the distal digits, including Hoxd13, Msx1, Lhx2, and Sox11 (*21–24*) (Fig. S1A). Our scRNA-seq analysis suggested that FW maintained the Distal and Proximal identities as they are, while NC drove both Distal and Proximal cells towards Proximal and “inactive” state aligning “Progress Zone model” in limb development (*25*) (Supplementary text, Fig. S2 and S3). Therefore, based on the cell lineages and expression profiles, FW sufficiently triggers the emergence of digit-like morphology in the three-dimensional culture of the cell aggregates (Hereafter we call it digit organoid), mimicking the developmental environment of the digit more faithfully than NC condition. Given that the differences in cell properties and cell sorting between Distal and Proximal cells

seem to play the central role in the pattern formation, it is difficult to reconcile that with the conventional Turing mechanism, prompting us to produce a new explanatory model based on cellular and molecular dynamics.

The cell adhesiveness and chemotaxis towards FW sufficiently explain the symmetry-breaking but not the elongation of the digit organoid.

To build an ABM explaining the mechanisms of symmetry-breaking and elongation in the digit organoids, we experimentally explored the cellular and molecular mechanisms during morphogenesis. Cell sorting is usually explained by differential cell adhesions. Indeed, EphA7 regulates the cell sorting between Distal and Proximal autopod mesenchyme at E11.5 mouse embryos (*18*). The cell adhesiveness can be visualized as an angle between doublets, such that the cells with stronger adhesion have shallower angles (*26*) (Fig. 2A, left schematic). Thus, we cultured aggregates of the Distal and Proximal cells separately in NC and FW conditions, dissociated on Day 1 and Day 2, made doublets, and measured the angles of the doublets (Fig. S4). The results showed that the cell adhesion between the Distal-Distal cells was stronger than the Distal-Proximal and the Proximal-Proximal on Day 1, and the Distal-Proximal adhesion became equally strong as the Distal-Distal on Day 2 when cultured in FW while there were no differences in cell adhesions when cultured in NC (Fig. 2A).

Based on the experimental results, we aimed to construct a minimal representative ABM computational model that highlights the critical biophysical mechanisms leading to the emergence of digits from a mixed aggregate of Distal and Proximal cells. By taking into account the differential adhesion such that the Distal-Distal adhesion is stronger than the Distal-Proximal or Proximal-Proximal, the Distal cells clustered at the center of the organoid, which is different from the experimental observation (Fig. 2B, dotted box).

In order for the Distal cells to cluster on the surface of the organoid, we supposed that Distal cells were directed towards the surface. We hypothesized that the signals from FW are the directional cues for the surface of the organoid. To test this possibility, we performed immunostaining against phosphorylated-ERK to visualize the cells activating Fgf signals in response to Fgf8b, and electroporated 7Tcf-GFP to visualize the cells activating canonical Wnt signals in response to Wnt3a. In both cases, the cells on the surface received the signals strongly (Fig. 2C).

It has been shown that limb mesenchyme are attracted towards the source of AER signals, especially Fgfs (*27*, *28*). Given that there was a gradient of the signals from FW towards the surface of the organoid, we tested whether the chemotaxis of Distal cells towards

the FW signals can explain the symmetry-breaking and elongation in ABM. Here, we did not assume that the cells have extracellular scaffolds for migration. Then, in order for the cells to exhibit directed migration towards the gradient, the cells need to pull the other cells back. Thus, we implemented that on top of the stronger base adhesion strength in the Distal cells, the Distal cells have directional traction bias against the Proximal cells towards the inner-outer gradient of FW (Fig. 2D). As a consequence, the ABM recapitulated the symmetry-breaking. However, in any case, the organoids could not exhibit elongation beyond the spherical clusters of the Distal cells (Fig. 2B, solid box).

Wnt5a regulates sustained elongation by convergent extension.

We hypothesized that the sustained elongation is regulated by the morphogen gradient secreted from Distal cells. To test the hypothesis, we electroporated Proximal cells with Distal morphogen candidate gene constructs: CAG-tagBFP-2A-Bmp2, -Bmp4, -Fgf10, -Inhba (encoding activin), and -Wnt5a, as well as -Hoxd13, which is considered to be the upstream of the Distal identity. We expected that if any of those genes neutralize the Distal-Proximal gradient of the morphogens, the elongation of the organoid would be inhibited, judged by the lower aspect ratios (the longest axis vs its orthogonal axis). Among them, the organoids expressing Hoxd13, Inhba, and Wnt5a showed a significant reduction in the aspect ratios (Fig. 3A, supplementary movie 4).

One might assume that the enhanced cell proliferation of the Distal cells can be an underlying mechanism of the elongation of Distal cell clusters. However, EdU incorporation experiments showed that although cell proliferations were promoted in FW condition compared to NC condition, and the proliferations were enhanced on Day 2 compared to Day 1 in both conditions, the Distal and Proximal cells had no significant difference in the rate of proliferation in each condition (Fig. 3B). These results suggested that another molecular mechanism is required to explain the sustained elongation of the Distal cell clusters.

When the tissue does not have any substrate to support its deformation outside of it, as long as the cells drive themselves towards the gradient, the cells pull the other cells back due to Newton's third law, and so the whole tissue cannot elongate towards the gradient. Instead, the cell needs to undergo convergent extension by pulling each other orthogonal direction to the gradient (*29*). Consistently, it has been shown that Wnt5a triggers planar cell polarity, which is necessary for convergent extension (*30–32*). Furthermore, the mechanical stress induced by convergent extension promotes the formation of activin, which organizes digit formations (*32*, *33*). We also confirmed that Distal cells expressed a higher amount of *Wnt5a*

(Fig. S5) and Wnt5a protein accumulated in the Distal part of the digit organoid (Fig. 3C). Thus, we hypothesize that accumulation of Wnt5a protein in Distal clusters triggers convergent extension.

To detect convergent extension quantitatively, we performed the live-imaging using a two-photon incubator microscope (*8*) and traced the cell trajectory in the four-dimensional images using TrackMate (*34*) and ELEPHANT (*35*) plug-in on ImageJ. Next, we computed the interpolated velocity vector field obtained from the tracks by Gaussian kernel smoothing. By following the flow of vector field, we obtained the deformation map of the organoid from which we computed the Cauchy-Green strain tensor. This measures how a reference sphere of cells in the initial frame of the experiment would deform when following the flow of the Distal and Proximal cells. After representing the deformed state by ellipses, the regions showing the convergent-extension can be detected as the ellipses with the longer axis along, and the shorter axis orthogonal to the axis of tissue elongation (Fig. 3D-F). We then plotted the primary axis of the deformation of ellipses projected to the elongation axis of the digit organoids. The results showed the maximal convergent extension where the difference in Wnt5a concentration is most elaborated at the Distal-Proximal interface (Fig. 3F).

The ABM revealed the minimum sufficient mechanisms for the morphogenesis of digit organoids

Grounded by the experimental evidence, we added another mechanism in ABM that when the Distal cells are among the Distal cells, the Distal cells have an adhesion bias orthogonal to the Wnt5a gradient, resulting in the convergent-extension cell motion (Fig. 4A, B). The ABM implementing the differential adhesions, Distal expression of Wnt5a gradient, chemotaxis, and convergent-extension successfully recapitulated the symmetry-breaking and elongation, suggesting that these are sufficient mechanisms explaining the digit morphogenesis in the digit organoids (Fig. 4C, solid box).

Now that we have built an ABM that recapitulates the tissue-level phenotype of the digit organoids, we aimed to further validate the model by direct comparison of the cell motions between the organoids and the ABM. Consistent with the experimental observation, the maximal convergent extension was detected at the Distal-Proximal cell interface in the ABM (Fig. 3F, 4D). In contrast, when only differential adhesion and FW-directed traction bias are implemented (Fig. 2D, solid box), the convergent extension maximum is weaker and co-localizes with Distal cluster (Fig. S6). The ABM also recapitulated that the number of protrusions increased as the initial number of the cells in the organoids increased (Fig. S7A,

top row). Furthermore, the ABM predicted that as the Proximal cell ratio increases, the protrusions increased (Fig. S7B, C). Consistently, the experiments showed that when the Distal cell ratio is higher, the Distal cell cluster does not bifurcate by itself. In contrast, when the Proximal cell ratio is higher, it increases the chance that the Distal cluster is separated (Fig S7D), further validating the ability of predicting tissue-level behaviors in the digit organoids by the ABM.

Our ABM is a high-dimensional dynamical system defined by four constitutive equations describing the evolution of a Distal cell position, a Proximal cell position, and Wnt5a and FW concentrations. The first equation indicates that the position of a Distal cell at the next moment is determined by the sum of two kinds of traction forces and one kind of repulsion forces. The Distal-Distal traction forces are computed as the sum of the vectors between the Distal cells within the distance R, weighted by the strong adhesion (ξ_{DD}: based on the doublet experiments) and the traction bias in the orthogonal way to Wnt5a gradient (for convergent extension). Likewise, the Distal-Proximal traction forces are computed as the sum of the vectors between the Proximal cells within R weighted by the modest adhesion (ξ_{DP}) and traction bias along FW gradient (for chemotaxis). The repulsion forces are for volume exclusions with the cells within the distance δ ($R > \delta$) (Fig. 4E, F). The position of a Proximal cell at the next moment can be computed in similar way, except the Proximal-Proximal traction forces are weighted by the weak adhesion (ξ_{PP}) and not biased by the gradient (Fig. 4G). The evolution of Wnt5a concentration is determined by the decay rate, the production rate determined by Distal cell density, and the slow diffusion within the organoid (Fig. 4H). The evolution of FW concentration is determined by the decay rate, the saturated diffusion outside the organoid, and the slow diffusion inside the organoid (Fig. 4J). As a result, the Wnt5a gradient is created at the Distal clusters.

Derivation of a PDE model shows fingering instability as a potential mathematical explanation for the emergence of "fingers".

Now that our ABM has sufficiently explained tissue-level observations, we explored a fundamental mathematical explanation for the emergence of digit morphologies. Based on the equations describing the dynamics of microscopic cell positions of Distal and Proximal cells, we derived PDEs describing the dynamics of Distal and Proximal cell densities by so-called mean-field limit approach (*36*), in which the organoid is broken down into infinite number ($N \to \infty$) of infinitely small ($R \equiv \varepsilon \to 0$) pieces (Fig. 5A-C, see Supplementary text for the mathematical details). After this limiting procedure, the organoid is solely described by two

densities ρ_D and ρ_P that can be interpreted as the probabilities to find Distal and Proximal cells at a specific location. Note that the force terms and their parameters in the ABM are essentially conserved in the PDE systems.

As the area where the cell density is not zero essentially means the shape of the tissues, the derived PDEs describe the evolution of tissue shapes. Although in general, PDEs can rarely be analytically solved, the forms of the equations sometimes indicate the fundamental nature of the dynamics. By expanding the force terms and organizing the equations as polynomials with respect to ε, we could obtain the PDE systems shown in Fig. 5D. Here, the terms with the lowest ε matter the most as we are considering ε as a much smaller number than 1. The dominating terms of order ε^{-1} were so-called advection terms, meaning the Distal density moves towards the direction of the gradient, while the Proximal density moves in the opposite way. These terms vanish when the Distal and Proximal densities are completely segregated, such that the probability of finding both Distal and Proximal cell types at the same location is zero ($\rho_D \rho_P = 0$) (Fig. 5D).

Subsequently, the equations turned out to be a modification of the Cahn–Hilliard equation—a well-known equation originally describing the behavior of interfaces between two fluids with different viscosities (*37–39*). For simplicity, we use FW and Wnt5a as the same given radial gradient ν and one (Distal) population. (Fig. 5E). Under certain conditions, such interfaces do not expand uniformly but instead form protrusions known as "fingering instability" (see Discussion) (*40*, *41*). The main finding of our PDE approach is that traction bias can be described by a new additional term to the standard Cahn-Hilliard equation. We showed that this modification is sufficient to trigger fingering-like instability (Fig. 5F). In more realistic setups mimicking situations of *in vivo* limb development where the morphogenesis is initiated from a hemispherical Distal tissue with unidirectional gradient ν, digit-like protrusions are formed in the distal direction (Fig. 5G). These results suggested that although the Distal tissue is not a viscous fluid, it behaves in a way that can be described by the same kind of PDE, eventually producing finger-like protrusions. Just as shown in the ABM, the number of the protrusions can be determined by the extent of the traction bias (η) and the size of the tissue (N) (Fig. F-I). Despite its name, as far as we know, fingering instability has never been applied to explain the development of "fingers", but taken altogether, our work implied that the emergence of "fingers" can be explained as fingering instability.

Discussion

To build an explanatory framework for the emergence of digit tissue morphologies, we developed a novel digit organoid in which the cell aggregate breaks its morphological symmetry and elongates into digit-like structures. Our examination of the molecular characterization suggested that our digit organoid reflects the extraction of essential cellular and molecular mechanisms of digit formation during development. The bottom-up approach using ABM showed that the tissue-level phenotypes of symmetry-breaking and tissue elongation in the digit organoid can be sufficiently explained by the inner-outer gradient of FW, differential adhesions, self-organization of Wnt5a gradient, chemotaxis, and convergent-extension, which were carefully validated by biological experiments. The derivation of PDE revealed that the fingering instability is an underlying analytical nature of the iterative processes in ABM, implying that the fingering instability is a fundamental mechanism for the emergence of digit morphologies.

Interestingly, the experiments in which the total number and the Distal/Proximal are modified in our model might be aligned with the mutant phenotypes of Hox genes and Gli3 (*17*). In Gli3 mutants in which the limb buds get larger, the digits are increased, consistent with larger organoids producing more digits-like protrusions (Fig. 1E, S1, S7A, top row). While the increment of the Distal cells does not increase the bifurcation of Distal clusters, the increment of the Proximal cells induced a higher number of digits in both the organoid and the simulation (Fig. S7A, middle row, B-D). In the mutant embryos, the complete knock-out of distal Hox genes abolishes any digit, consistent with no Distal cells in the organoid. The partial knock-out of distal Hox genes increases the number of digits, consistent with less Distal cells in the organoid producing more digits (Supplementary Fig. S7).

Fingering instability is a mechanical mechanism for patterning that differs fundamentally from the widespread Turing models. Of note, this study does not necessarily disprove the Turing models. In this study, we did not extensively analyze the biochemical interactions among the cells besides Wnt5a and their relations with cartilage differentiation of the cells during the cartilage patterning, although the accumulation of the Distal cells coincided with the cartilage differentiation and the initiation of formation of digit-like structures. At this point, Turing models and our models are two different simplified representations of the complex biological processes of limb morphogenesis. However, the strength of our model is that it is grounded in directly observable microscopic behaviors of cells and molecules. It would be interesting to analyze the signaling interactions while tracking the motions of

individual cells, then that might reveal if both models are proven to be two sides of the same coin and integrable, or one disproves the other.

Recently, a growing number of studies leveraging multicellular *in vitro* models have revealed mechanisms of the emergent property of tissue morphogenesis. For instance, in the epithelial tissues such as the optic cup and the intestinal crypt, in which morphogenesis can be understood as deformation of the sheet, the interactions between the mechanical properties of the tissues and the cell fates sufficiently explain the program of self-organizing morphogenesis (*8*, *42–45*). Those understandings have enabled robust and precise controls in tissue engineering (*46*, *47*). As mesenchymal tissues, "gastruloid" modeling the development of growing axial tissues shows similar morphological phenotypes as our model, including symmetry-breaking and elongation, based on the differential adhesions and convergent extension (*48–50*). Thus, it would be interesting to test to what extent the variety of tissue morphologies can be explained by the current understanding of morphological programs, with the variations of parameters and combinations of the epithelial and mesenchymal programs.

As mentioned above, fingering instability typically describes the behaviors of the interface where a less viscous fluid displaces a more viscous one, or vice versa. Generally, the fluid interface tends to be round or flat due to the surface tension (stability), but by coupled with the factors to expand, the interface creates protrusions (fingering). The key here is a mathematical balance between the stabilizing and expansion factors often described as Cahn-Hilliard and some additional terms. Although fingering instability based on the Cahn-Hilliard equation has never been applied to explain the development of "fingers", it has been applied to explain biological systems such as tumor growth, expansion of epithelial colonies, and formation of intestinal villi (*51–53*). A further implication of this work is that the same framework might be applied to many other developmental situations where the tissue deformation is driven by convergent-extension.

Importantly, the parameters in our PDE are conserved from the ABM. Therefore, the parameters governing the tissue-level phenotypes can be potentially empirically determined by experiments. That might reveal the underlying mechanisms, the conservation, and variation of the digit numbers. For instance, although the number of digits is determined by the size of the limb bud in mice, and the sizes of the limb bud vary by species, the five digits are a robustly conserved phenotype among extant tetrapods (*54*). Although some animals exhibit the digit reduction by add-hock developmental mechanisms (*55*, *56*), virtually no extant animal species

has more than five digits. The empirical mechanisms of this strangely conserved phenotype, often regarded as a developmental constraint, might be explained by rigorously characterizing the relationship between the microscopic developmental parameters and macroscopic tissue morphologies. Overall, we believe this work paves the way for uncovering unexplained mechanisms of phenotypic variations in tissue morphologies and also for precision tissue engineering strategies.

1. M. Logan, H. G. Simon, C. Tabin, Differential regulation of T-box and homeobox transcription factors suggests roles in controlling chick limb-type identity. *Development* **125**, 2825–2835 (1998).

2. H. Ohuchi, J. Takeuchi, H. Yoshioka, Y. Ishimaru, K. Ogura, N. Takahashi, T. Ogura, S. Noji, Correlation of wing-leg identity in ectopic FGF-induced chimeric limbs with the differential expression of chick Tbx5 and Tbx4. *Development* **125**, 51–60 (1998).

3. D. M. Wellik, M. R. Capecchi, Hox10 and Hox11 genes are required to globally pattern the mammalian skeleton. *Science* **301**, 363–367 (2003).

4. C. Fromental-Ramaint, X. Warott, N. Messadecq, M. LeMeur, P. Dolle, P. Chambon, Hoxa-13 and Hoxd-13 play a crucial role in the patterning of the limb autopod. *Development* **122**, 2997–3011 (1995).

5. P. W. Anderson, More Is Different. *Science* **177**, 393–396 (1972).

6. Y. Sasai, Cytosystems dynamics in self-organization of tissue architecture. *Nature* **493**, 318–326 (2013).

7. A. Warmflash, B. Sorre, F. Etoc, E. D. Siggia, A. H. Brivanlou, A method to recapitulate early embryonic spatial patterning in human embryonic stem cells. *Nat. Methods* **11**, 847–854 (2014).

8. M. Eiraku, N. Takata, H. Ishibashi, M. Kawada, E. Sakakura, S. Okuda, K. Sekiguchi, T. Adachi, Y. Sasai, Self-organizing optic-cup morphogenesis in three-dimensional culture. *Nature* **472**, 51 (2011).

9. M. Eiraku, K. Watanabe, M. Matsuo-Takasaki, M. Kawada, S. Yonemura, M. Matsumura, T. Wataya, A. Nishiyama, K. Muguruma, Y. Sasai, Self-Organized Formation of Polarized Cortical Tissues from ESCs and Its Active Manipulation by Extrinsic Signals. *Cell Stem Cell* **3**, 519–532 (2008).

10. A. M. De Lise, E. Stringa, W. A. Woodward, M. A. Mello, R. S. Tuan, "Embryonic Limb Mesenchyme Micromass Culture as an In Vitro Model for Chondrogenesis and Cartilage Maturation" in *Developmental Biology Protocols*, R. S. Tuan, C. W. Lo, Eds. (Humana Press, Totowa, NJ, 2000; https://doi.org/10.1385/1-59259-066-7:359), pp. 359–375.

11. M. Weisberg, *Simulation and Similarity: Using Models to Understand the World* (Oxford University Press, Oxford, Reprint edition., 2015).

12. J. Raspopovic, L. Marcon, L. Russo, J. Sharpe, Digit patterning is controlled by a Bmp-Sox9-Wnt Turing network modulated by morphogen gradients. *Science* **345**, 566–570 (2014).

13. A. M. Turing, The chemical basis of morphogenesis. *Bull. Math. Biol.* **52**, 153–197 (1990).

14. D. ten Berge, S. A. Brugmann, J. A. Helms, R. Nusse, Wnt and FGF signals interact to coordinate growth with cell fate specification during limb development. *Development* **135**, 3247–3257 (2008).

15. C. Duarte-Olivenza, J. M. Hurle, J. A. Montero, C. I. Lorda-Diez, Modeling the Differentiation of Embryonic Limb Chondroprogenitors by Cell Death and Cell Senescence in High Density Micromass Cultures and Their Regulation by FGF Signaling. *Cells* **12**, 175 (2023).

16. D. Kumar, A. B. Lassar, Fibroblast Growth Factor Maintains Chondrogenic Potential of Limb Bud Mesenchymal Cells by Modulating DNMT3A Recruitment. *Cell Rep.* **8**, 1419–1431 (2014).

17. R. Sheth, L. Marcon, M. F. Bastida, M. Junco, L. Quintana, R. Dahn, M. Kmita, J. Sharpe, M. A. Ros, Hox Genes Regulate Digit Patterning by Controlling the Wavelength of a Turing-Type Mechanism. *Science* **338**, 1476–1480 (2012).

18. H. S. Stadler, K. M. Higgins, M. R. Capecchi, Loss of Eph-receptor expression correlates with loss of cell adhesion and chondrogenic capacity in Hoxa13 mutant limbs. *Development* **128**, 4177–4188 (2001).

19. A. M. Fuiten, Y. Yoshimoto, C. Shukunami, H. S. Stadler, Digits in a dish: An in vitro system to assess the molecular genetics of hand/foot development at single-cell resolution. *Front. Cell Dev. Biol.* **11** (2023).

20. M. Honda, S. Oki, R. Kimura, A. Harada, K. Maehara, K. Tanaka, C. Meno, Y. Ohkawa, High-depth spatial transcriptome analysis by photo-isolation chemistry. *Nat. Commun.* **12**, 4416 (2021).

21. S. Bruneau, K. R. Johnson, M. Yamamoto, A. Kuroiwa, D. Duboule, The Mouse *Hoxd13*spdh Mutation, a Polyalanine Expansion Similar to Human Type II Synpolydactyly (SPD), Disrupts the Function but Not the Expression of Other *Hoxd* Genes. *Dev. Biol.* **237**, 345–353 (2001).

22. D. Houzelstein, A. Cohen, M. E. Buckingham, B. Robert, Insertional mutation of the mouse *Msx1* homeobox gene by an *nlacZ* reporter gene. *Mech. Dev.* **65**, 123–133 (1997).

23. I. Tzchori, T. F. Day, P. J. Carolan, Y. Zhao, C. A. Wassif, L. Li, M. Lewandoski, M. Gorivodsky, P. E. Love, F. D. Porter, H. Westphal, Y. Yang, LIM homeobox transcription factors integrate signaling events that control three-dimensional limb patterning and growth. *Development* **136**, 1375–1385 (2009).

24. M. Hargrave, E. Wright, J. Kun, J. Emery, L. Cooper, P. Koopman, Expression of the Sox11 gene in mouse embryos suggests roles in neuronal maturation and epithelio-mesenchymal induction. *Dev. Dyn.* **210**, 79–86 (1997).

25. D. Summerbell, J. H. Lewis, L. Wolpert, Positional Information in Chick Limb Morphogenesis. *Nature* **244**, 492–496 (1973).

26. J.-L. Maître, H. Berthoumieux, S. F. G. Krens, G. Salbreux, F. Jülicher, E. Paluch, C.-P. Heisenberg, Adhesion Functions in Cell Sorting by Mechanically Coupling the Cortices of Adhering Cells. *Science* **338**, 253–256 (2012).

27. S. Li, K. Muneoka, Cell Migration and Chick Limb Development: Chemotactic Action of FGF-4 and the AER. *Dev. Biol.* **211**, 335–347 (1999).

28. J. Gros, J. K.-H. Hu, C. Vinegoni, P. F. Feruglio, R. Weissleder, C. J. Tabin, WNT5A/JNK and FGF/MAPK Pathways Regulate the Cellular Events Shaping the Vertebrate Limb Bud. *Curr. Biol.* **20**, 1993–2002 (2010).

29. G. Lesnicar-Pucko, J. M. Belmonte, M. Musy, J. A. Glazier, J. Sharpe, Cellular mechanisms of chick limb bud morphogenesis. *bioRxiv*, 2020.09.10.292359 (2020).

30. B. Gao, H. Song, K. Bishop, G. Elliot, L. Garrett, M. A. English, P. Andre, J. Robinson, R. Sood, Y. Minami, A. N. Economides, Y. Yang, Wnt Signaling Gradients Establish Planar Cell Polarity by Inducing Vangl2 Phosphorylation through Ror2. *Dev. Cell* **20**, 163–176 (2011).

31. B. Gao, R. Ajima, W. Yang, C. Li, H. Song, M. J. Anderson, R. R. Liu, M. B. Lewandoski, T. P. Yamaguchi, Y. Yang, Coordinated directional outgrowth and pattern formation by integration of Wnt5a and Fgf signaling in planar cell polarity. *Development* **145**, dev163824 (2018).

32. C. Parada, S. P. Banavar, P. Khalilian, S. Rigaud, A. Michaut, Y. Liu, D. M. Joshy, O. Campàs, J. Gros, Mechanical feedback defines organizing centers to drive digit emergence. *Dev. Cell* **57**, 854-866.e6 (2022).

33. J. A. Montero, C. I. Lorda-Diez, Y. Gañan, D. Macias, J. M. Hurle, Activin/TGFβ and BMP crosstalk determines digit chondrogenesis. *Dev. Biol.* **321**, 343–356 (2008).

34. J.-Y. Tinevez, N. Perry, J. Schindelin, G. M. Hoopes, G. D. Reynolds, E. Laplantine, S. Y. Bednarek, S. L. Shorte, K. W. Eliceiri, TrackMate: An open and extensible platform for single-particle tracking. *Methods* **115**, 80–90 (2017).

35. K. Sugawara, Ç. Çevrim, M. Averof, Tracking cell lineages in 3D by incremental deep learning. *eLife* **11**, e69380 (2022).

36. L.-P. Chaintron, A. Diez, Propagation of chaos: A review of models, methods and applications. I. Models and methods. *Kinet. Relat. Models* **15**, 895–1015 (2022).

37. N. J. Armstrong, K. J. Painter, J. A. Sherratt, A continuum approach to modelling cell–cell adhesion. *J. Theor. Biol.* **243**, 98–113 (2006).

38. C. Falcó, R. E. Baker, J. A. Carrillo, A Local Continuum Model of Cell-Cell Adhesion. *SIAM J. Appl. Math.* **84**, S17–S42 (2024).

39. I. Kim, A. Mellet, J. Sheung-Him Wu, "Aggregation-Diffusion Phenomena: From Microscopic Models to Free Boundary Problems" in *Active Particles, Volume 4* (Birkhäuser, Cham, 2024; https://link.springer.com/chapter/10.1007/978-3-031-73423-6_6), pp. 217–281.

40. P. G. Saffman, G. I. Taylor, The penetration of a fluid into a porous medium or Hele-Shaw cell containing a more viscous liquid. *Proc. R. Soc. Lond. Ser. Math. Phys. Sci.* **245**, 312–329 (1997).

41. J. W. Cahn, J. E. Hilliard, Free Energy of a Nonuniform System. I. Interfacial Free Energy. *J. Chem. Phys.* **28**, 258–267 (1958).

42. S. Okuda, N. Takata, Y. Hasegawa, M. Kawada, Y. Inoue, T. Adachi, Y. Sasai, M. Eiraku, Strain-triggered mechanical feedback in self-organizing optic-cup morphogenesis. *Sci. Adv.* **4**, eaau1354 (2018).

43. C. Pérez-González, G. Ceada, F. Greco, M. Matejčić, M. Gómez-González, N. Castro, A. Menendez, S. Kale, D. Krndija, A. G. Clark, V. R. Gannavarapu, A. Álvarez-Varela, P. Roca-Cusachs, E. Batlle, D. M. Vignjevic, M. Arroyo, X. Trepat, Mechanical compartmentalization of the intestinal organoid enables crypt folding and collective cell migration. *Nat. Cell Biol.* **23**, 745–757 (2021).

44. Q. Yang, S.-L. Xue, C. J. Chan, M. Rempfler, D. Vischi, F. Maurer-Gutierrez, T. Hiiragi, E. Hannezo, P. Liberali, Cell fate coordinates mechano-osmotic forces in intestinal crypt formation. *Nat. Cell Biol.* **23**, 733–744 (2021).

45. D. Serra, U. Mayr, A. Boni, I. Lukonin, M. Rempfler, L. Challet Meylan, M. B. Stadler, P. Strnad, P. Papasaikas, D. Vischi, A. Waldt, G. Roma, P. Liberali, Self-organization and symmetry breaking in intestinal organoid development. *Nature* **569**, 66–72 (2019).

46. N. Gjorevski, M. Nikolaev, T. E. Brown, O. Mitrofanova, N. Brandenberg, F. W. DelRio, F. M. Yavitt, P. Liberali, K. S. Anseth, M. P. Lutolf, Tissue geometry drives deterministic organoid patterning. *Science* **375**, eaaw9021 (2022).

47. M. Nikolaev, O. Mitrofanova, N. Broguiere, S. Geraldo, D. Dutta, Y. Tabata, B. Elci, N. Brandenberg, I. Kolotuev, N. Gjorevski, H. Clevers, M. P. Lutolf, Homeostatic mini-intestines through scaffold-guided organoid morphogenesis. *Nature* **585**, 574–578 (2020).

48. S. C. van den Brink, P. Baillie-Johnson, T. Balayo, A.-K. Hadjantonakis, S. Nowotschin, D. A. Turner, A. M. Arias, Symmetry breaking, germ layer specification and axial organisation in aggregates of mouse embryonic stem cells. *Development* **141**, 4231–4242 (2014).

49. M. A. de Jong, E. Adegeest, N. M. L. P. Bérenger-Currias, M. Mircea, R. M. H. Merks, S. Semrau, The shapes of elongating gastruloids are consistent with convergent extension driven by a combination of active cell crawling and differential adhesion. *PLOS Comput. Biol.* **20**, e1011825 (2024).

50. H. M. McNamara, S. C. Solley, B. Adamson, M. M. Chan, J. E. Toettcher, Recording morphogen signals reveals mechanisms underlying gastruloid symmetry breaking. *Nat. Cell Biol.* **26**, 1832–1844 (2024).

51. T. R. Huycke, T. J. Häkkinen, H. Miyazaki, V. Srivastava, E. Barruet, C. S. McGinnis, A. Kalantari, J. Cornwall-Scoones, D. Vaka, Q. Zhu, H. Jo, R. Oria, V. M. Weaver, W. F. DeGrado, M. Thomson, K. Garikipati, D. Boffelli, O. D. Klein, Z. J. Gartner, Patterning and folding of intestinal villi by active mesenchymal dewetting. *Cell* **187**, 3072-3089.e20 (2024).

52. M. Ebenbeck, H. Garcke, R. Nürnberg, Cahn–Hilliard–Brinkman systems for tumour growth. *Discrete Contin. Dyn. Syst. - S* **14**, 3989–4033 (2021).

53. Y. Ye, J. Lin, Fingering Instability Accelerates Population Growth of a Proliferating Cell Collective. *Phys. Rev. Lett.* **132**, 018402 (2024).

54. F. Galis, J. J.M. van Alphen, J. A.J. Metz, Why five fingers? Evolutionary constraints on digit numbers. *Trends Ecol. Evol.* **16**, 637–646 (2001).

55. K. L. Cooper, K. E. Sears, A. Uygur, J. Maier, K.-S. Baczkowski, M. Brosnahan, D. Antczak, J. A. Skidmore, C. J. Tabin, Patterning and post-patterning modes of evolutionary digit loss in mammals. *Nature* **511**, 41–45 (2014).

56. J. Lopez-Rios, A. Duchesne, D. Speziale, G. Andrey, K. A. Peterson, P. Germann, E. Ünal, J. Liu, S. Floriot, S. Barbey, Y. Gallard, M. Müller-Gerbl, A. D. Courtney, C. Klopp, S. Rodriguez, R. Ivanek, C. Beisel, C. Wicking, D. Iber, B. Robert, A. P. McMahon, D. Duboule, R. Zeller, Attenuated sensing of SHH by Ptch1 underlies evolution of bovine limbs. *Nature* **511**, 46–51 (2014).

57. S. Markman, M. Zada, E. David, A. Giladi, I. Amit, E. Zelzer, A single-cell census of mouse limb development identifies complex spatiotemporal dynamics of skeleton formation. *Dev. Cell*, doi: 10.1016/j.devcel.2023.02.013 (2023).

Figure 1. **Cell sorting between Distal and Proximal cells governs pattern formation in micromass and digit organoid cultures.** (A) Micromass culture of limb mesenchyme (E11.5) in NC and FW at 72 h; Sox9-GFP in white; Distal and Proximal cells labeled with H2BtdTomato (green) and H2BtagBFP (magenta). (B) Dot plots of Sox9-GFP intensity over time in Distal (left) and Proximal (right) cells; points colored by the number of Distal neighbors among the 10 nearest. (C) Violin/box plots at 72 h comparing neighbor groups (≥9 vs ≤1 Distal neighbors) within each cell type using two-tailed unpaired Student's t-tests; significance shown as asterisks ($p<0.05$, $*p<0.01$, $**p<0.001$). Percentages per group are shown below; sample sizes (n) and means are annotated. (D) Average Nearest Neighbor Score (NNS, k=10) over time in NC and FW, defined as the proportion of same-type neighbors normalized by cell-type frequency; lines show means, ribbons show bootstrapped 95% CIs. (E–G) Digit organoids in NC or FW for 193 h initiated from 9,000 or 27,000 cells. (E) Sox9-GFP (green) over bright-field overlays at 193h. (F) Distal/Proximal labeling with H2BVenus (green) and H2BtdTomato (magenta) at 76h. (G) time-lapse in FW (9,000 cells).

Figure S1. **The starting number of cells affected the number of protrusions.** Stacked bar charts show the percentage of colonies with a given number of protrusions across starting-cell groups; segment labels are raw counts and x-axis ticks show total n per group. Association between starting cell number and protrusion-category distribution was tested using a batch-stratified Cochran–Mantel–Haenszel (CMH) test, restricted to 2 batches containing ≥2 starting-cell groups: CMH $M^2 = 28.07$, df = 10, p = 0.00176 (two-sided, α = 0.05). Percentages in bars are descriptive.

Figure S2. **Distal–Proximal gene programs in digit organoids (FW).** (A) Volcano plot comparing tip (Distal) vs bottom (Proximal) PIC profiles; x = $\log_2$FC, y = $-\log_{10}$(p). Genes called Tip (red) if $\log_2$FC > 0.6 & p < 0.05, Bottom (blue) if $\log_2$FC < −0.6 & p < 0.05; others black. Vertical lines ±0.6 (~1.5-fold); horizontal line p = 0.05; significant genes labeled. (B) UMAP of scRNA-seq: Day 1 (red), Day 2 (blue). (C) Marker table for surface ectoderm, AER, limb mesenchyme: % cells with ≥1 UMI; summary row shows % cells with ≥2 markers/tissue. (D) DotPlot of these markers across clusters (Day1/Day2 Distal/Proximal; muscles): dot size = %≥1 UMI; color = scaled mean. (E–F) UMAP FeaturePlots of Distal_Score (average of top 20 tip-enriched genes from A; magenta→green) and Proximal_Score (top 20 bottom-enriched; green→magenta). (G) UMAP annotated by Day and Distal/Proximal using B, E–F. (H) RNA-velocity streamlines (scVelo). (I) Slingshot principal curves, rooted as in H, with endpoints Day2_FW_Distal_2 (lineage 1: Distal) and Day2_FW_Proximal (lineage 2: Proximal). (J) For selected genes (Wnt5a, Fgf10, Inhba, Bmp2/4, Hoxd13): top, UMAP colored by log(expression+1) with Slingshot curves; bottom, log(expression+1) vs Slingshot pseudotime per lineage (Distal: purple, Proximal: yellow) with tradeSeq NB-GAM smoothers.

Figure S3. **FW condition maintains Distal identity and an "active" state.** (A) UMAP of digit organoids (FW/NC; Day 1/Day 2) together with E11.5 Distal/Proximal cells (Day 0), annotated by DNA–lipid barcoding and Fig. S2G. (B–C) FeaturePlots of per-cell module scores on the UMAP. The FW signature is the average expression of the top 50 genes up-regulated in Day1_FW vs Day2_NC (Wilcoxon FindMarkers, padj < 0.05); the NC signature is the

corresponding NC-up set. Scores are shown per cell with truncated scales (10th–90th percentiles): (B) FW signature (green→magenta), (C) NC signature (magenta→green). (D) Violin/box plots of the FW signature across binned clusters (Day1-/Day2-FW-Distal, Day1-/Day2-FW-Proximal, Day1-/Day2-NC); white dots mark medians. Pairwise two-sided Wilcoxon rank-sum tests; Benjamini–Hochberg–adjusted p-values are shown above brackets. x-axis labels include per-bin sample sizes (n); values are module-score units. (E) Schematic: FW sustains Distal identity and an "active" program. (F–G) Metacell scatter (Markman et al., 2023): x = FW module score, y = NC module score. (F) Colored by metacell class (P1 naïve, P3 autopodial, P2 proximal progenitors; CT0–CT2 connective tissue/tendon; C1–C6 chondrocyte states; Attachment). (G) Same scatter colored by developmental time (E10.5–E14.5; majority vote per metacell).

Figure 2. **Differential adhesion + FW-directed traction bias explain symmetry breaking.** (A) Beeswarm + box plots of Angle by doublet class—Distal–Distal (DD), Distal–Proximal (DP), Proximal–Proximal (PP)—for Day1/Day2 NC and Day1/Day2 FW. Each dot is one doublet; point shape = Batch. Statistics: one-way ANOVA per experiment (Angle ~ Doublet); if significant ($\alpha = 0.05$), Tukey's HSD pairwise tests were run; labels above brackets report Tukey-adjusted p values (two-sided). (B) Agent-based model with differential adhesion (DD > DP > PP) and a traction bias toward FW (outer→inner). Axes: α, adhesion contrast; η, traction bias. Dotted box: adhesion-only. Solid box: adhesion + traction with an inset showing outline of a protrusion (dotted). (C) Day-1 FW organoid immunostaining of dpERK and 7Tcf-EGFP (anti-GFP). Signal intensity is mapped red→blue (high→low). (D) Schematic of the model rules. Left: x, overall cell–cell traction force; y, angle (°) between the pair axis and the FW gradient. DD (green: strong) and PP (magenta: weak) traction forces are constant; DP (yellow) traction forces are determined by their angle to the FW gradient. Dotted box: The biased DP traction vectors (blue arrows) yield Distal motion towards FW gradient (black arrowhead). Solid box: predicted tissue-level Distal motion toward the FW gradient (black arrowheads).

Figure S4. **Doublet assay workflow**. Distal and Proximal cell aggregates were cultured in FW, dissociated on Day 1 or Day 2, and membrane-labeled with MemGlow dyes (488 or 560). Doublets were then assembled in predefined pairings: Distal_488–Distal_560 (DD), Distal_560–Proximal_488 (DP), and Proximal_488–Proximal_560 (PP).

Figure 3. **Wnt5a expression in Distal cells and convergent extension.** (A) Overexpression screen in Proximal cells. Box–jitter plots show organoid aspect ratio by gene (x); each dot is one aggregate (shape = Batch). Control = tagBFP-only; constructs express Bmp2, Bmp4, Fgf10, Hoxd13, Inhba, Wnt5a. Statistics: planned two-sided t-tests vs Control; unadjusted p values are printed above brackets. (B) EdU incorporation (% EdU^+) in Distal (green) vs Proximal (magenta) cells on Day 1/Day 2 under NC and FW. Bars show means; dots are individual samples (shape = Batch). Two-sided unpaired t-tests (Distal vs Proximal); unadjusted p values shown. (C) Day-2 FW organoid immunostaining of Wnt5a (green) with DAPI (blue). (D–F) Convergent-extension (CE) analysis. (D) Workflow: tracked cell positions are smoothed into a velocity field and integrated to estimate tissue deformation; from this, the

primary axis of extension and its strength are extracted and visualized as deformation of a reference spheres into ellipses (See supplementary document). (E) Representative CE analysis from experimental data. (F) CE vectors projected along the tissue-elongation axis are plotted versus positions on the tissue-elongation axis (red) and overlaid with Distal (green) and Proximal (magenta) cell-density profiles, highlighting regions where CE occurs.

Figure S5. **Relative *Wnt5a* expression (qPCR) in 2D micromass, Day 1.** Box–dot plots show relative *Wnt5a* expression for four groups: Day1_FW_Distal, Day1_FW_Proximal, Day1_NC_Distal, Day1_NC_Proximal on 2D micromass culture. Each dot is one sample (biological replicate). The y-axis shows normalized expression by internal control (*Gapdh*). One-way ANOVA across the four groups, with Tukey's HSD for pairwise comparisons. Planned contrasts (Distal vs Proximal within FW and within NC) were tested by two-sided t-tests; unadjusted p values are printed on the plot.

Figure 4. **Sufficient conditions to explain tissue deformation in ABM** (A) Rule map: x = pair traction; y = angle to the gradient. DD traction is strongest orthogonal to Wnt5a; DP is strongest along FW; PP is weak/constant. Dotted boxes show traction biases in DD and DP cases. (B) Tissue-scale CE: Distal motion orthogonal to the Wnt5a gradient drives elongation. (C) ABM combining differential adhesion (DD>DP>PP), DP bias toward FW, Distal Wnt5a production, and DD bias orthogonal to Wnt5a. Parameters: α (adhesion differences) vs η (traction bias); solid box marks protrusion shape (dotted line in inset). (D) CE vectors of ABM simulations projected onto the elongation axis. (E) Schematic for F: neighbors within diameter *R* exert identity-/gradient-dependent tractions; short-range repulsion prevents overlap; labels link terms to the equations. (F) Evolution of Distal cell position: sum of DD/DP tractions with the above angle biases plus repulsion within δ. (G) Evolution of Proximal cell position: sum of PP/DP tractions plus repulsion within δ. (H) Evolution of Wnt5a concentration: Distal production, slow diffusion, and decay. (I) Evolution of FW concentration: slow diffusion with decay inside organoids and a saturated external reservoir, forming an inner–outer gradient. (J) Overview of gradients in H–I.

Figure S6. **CE index in an ABM with differential adhesion and FW-directed traction bias.** The solid red curve shows the CE index projected onto the tissue-elongation (AP) axis; the gray dashed curve shows the orthogonal component. Shaded green and magenta bands are kernel-density estimates of Distal and Proximal cells, respectively (four time points). The AP-aligned CE peak is modest and spatially coincident with Distal cluster, unlike the larger peaks at the interface between Distal and Proximal clusters in Figs. 3F and 4D where Wnt5a-induced/orthogonal biases are included.

Figure S7. **Parameters regulating protrusion number.** (A) ABM parameters controlling protrusions. Predicted protrusion number varies with (i) traction bias toward FW (η), (ii) Distal cell fraction (D/(D+P)), and (iii) total cell number (N). The panel summarizes how changes in these parameters shift the distribution of protrusions. (B-D) Starting composition vs protrusions. Left: Stacked bars show the percentage of organoids with 0, 1, 2, or 3 protrusions for each starting condition (Dxxxx_Pyyyy; D = Distal cells, P = Proximal cells). Numbers

inside segments = raw counts; x-axis labels include total n; y-axis = %. Colors (0–3) are consistent across panels. Right: Representative images at 72 h; each image is annotated with the starting condition and D:P ratio. (A) Group 1 (P fixed at 6,000): D3000_P6000, D6000_P6000, D9000_P6000. (B) Group 2 (P fixed at 12,000): D6000_P12000, D12000_P12000, D18000_P12000. (C) Group 3 (P increased): D3000_P6000, D3000_P18000, D9000_P18000. (D)

Figure 5. **Fingering instability in PDE models.** (A) Derivation scheme. The ABM is coarse-grained by letting cell number N→∞ with small size ε, yielding Distal and Proximal densities (tissue shapes). For simplicity, FW and Wnt5a gradients are given as the same radial gradient ν. (B) Microscopic rule recap: Distal/Proximal positions evolve by pairwise tractions plus short-range repulsion. (C) Corresponding density evolutions inherit those traction (dark/light blue) and repulsion (red) effects. (D) Advection terms at dominant order ε^{-1}: Distal tissue drifts up ν and Proximal tissue away from it; cartoons illustrate the motions. (E) Cahn–Hilliard term (CH) at next order ε^{0}: the Distal PDE contains a CH term with a novel anisotropic diffusion operator arising from biased tractions. (F) Simulation endpoints at time T across total size N and traction bias η. (G) Simulations in *in vivo*-like setups initiated from hemispherical Distal tissues with a unidirectional ν. (H) Protrusion number vs η. The normalized largest boundary Fourier mode c_k/c_0 increases with η (shown for each N; values capped at 0.05). (I) Protrusion number vs N. Heat map of the first 12 Fourier modes (max normalized to 1) versus N at η = 0.6, indicating more fingers as N grows.

Acknowledgement

We thank all members of the Eiraku Lab for helpful discussions; Dr. Hitomi Watanabe for generating Sox9–GFP mouse embryos; and Dr. Ko Sugawara for technical support with the ELEPHANT plug-in. We thank Single-cell Genome Information Analysis Core (SignAC) at WPI-ASHBi, Kyoto University for their support. This work was supported by ASHBi Fusion Reseach Grant (FY2023-2024: to R.T, S.P., and A.D.), Japan Society for the Promotion of Science (JSPS) Grant-in-Aid for Research Activity Start-up (JP20K22652 to R.T.), Grant-in-Aid for Early-Career Scientists (JP22K15122 to R.T.), KAKENHI Grant-in-Aid for Early-Career Scientists (JP23K13015 to A.D., JP24K16962 to S.P.), Grant-in-Aid for Transformative Research Areas (Ministry of Education, Culture, Sports, Science, and Technology, MEXT), Japan (JP23H04933 to M.E., JP22H05110 supporting S.P.), and Core Research for Evolutional Science and Technology (CREST, JST) (JPMJCR12W2 to M.E.).

Supplementary text for scRNA-seq

To analyze the expression dynamics of the secreted molecules from Distal cells, we first focused on scRNA-seq profiles from digit organoids grown in FW condition collected on Day 1 and Day 2 (Day1_FW and Day2_FW), which were segregated on UMAP space (Fig. S2B). To confirm that epidermal contribution was effectively minimized, surface ectoderm and AER markers (Epcam, Cdh1, Wnt6, Krt8/18, Fgf8, Wnt3a, Krt5/14, Trp63) were detected in only a very small minority of cells, with only 2.64% and 0.172% of cells expressing more than 2 surface ectoderm or AER markers, respectively. In contrast, mesenchymal limb bud markers (Prrx1, Hand2, Tbx5, Pdgfra, Hoxa13) were robustly expressed in 55–95% of cells, and 91% of cells expressed more than two mesenchymal markers (Fig. S2C, D). To characterize Distal and Proximal cells, we picked up top 20 differentially expressed genes (DEGs) between the tip and the bottom of the organoid from the PIC experiments (Fig. S2A) and computed the normalized average expression levels of those genes as “Distal Score” and “Proximal Score”, respectively Fig. S2E, F). As the results suggested that the cell clusters in the top half on the UMAP were Distal cells, we annotated Day1_FW_Distal, Day2_FW_Distal, Day1_FW_Proximal, and Day2_FW_Proximal clusters on the UMAP (Fig. S2G). Based on this information, we generated the pseudo-trajectory using RNA velocity and slingshot (Fig. 2H, I). Subsequently, we inferred the expression dynamics of the genes that are upregulated in the Distal lineage, such as Bmp2, Bmp4, Hoxd13, Wnt5a, Fgf10, and Inhba.

Next, to get some insight into the role of FW in in vitro culture, we mapped the cell clusters annotated above onto a larger data set including Distal and Proximal limb autopod mesenchyme at E11.5 (Day0_Distal, Day0_Proximal), which are the source cells of the organoids, as well as the cells from organoids grown in NC condition collected on Day1 and 2 (Day1_NC, Day2_NC) (Fig. S3A). We picked up the top 50 DEGs between {Day1_FW and Day2_FW} vs {Day1_NC and Day2_NC} and computed the normalized average expression levels of those genes as “FW signature” and “NC signature”. In both plots, we validated that the cells high in the FW signature and low in the NC signature (both colored in green) overlapped with the cells cultured in FW conditions (Fig. S3B, C). Interestingly, Day0_Distal cells also turned on green on both plots, suggesting that the difference between the cells cultured in FW and NC conditions correlated with the distal-proximal difference in the limb bud (Fig. S3B, C). The violin plot for the FW signature further showed that FW_Distal are highest in the FW signature, FW_Proximal cells come next, and NC cells are lowest (Fig. S3D). These results implied that as “Progress Zone model” in limb development (*25*) proposed, FW,

namely AER signals maintain the cells as Distal and “active” state, while the cells deprived of AER signals become Proximal and “inactive” state (Fig. S3E).

Re-analysis of the scRNA-seq data from Markman et al. 2023 (*57*) further confirmed that the metacells assigned as “Naive progenitors,” “Autopodial progenitors”, were “Proximal progenitors” were high in FW signature and low in NC signature, while the cells assigned as “Mature chodrocytes”, “Mature autopodial chodrocytes”, and “Intermediate autopodial cells” were high in NC signature and low in FW signature (Fig. S3F). The correlation of FW and NC signatures with “active” and “inactive” is also represented by the plot showing the metacells assigned as earlier stages were higher in FW signature and lower in NC signature (Fig. S3G). Taken together, our scRNA-seq results suggested that FW conditions maintained the Distal and Proximal identities as undifferentiated mesenchyme while NC conditions drives both of the cells towards more Proximal and differentiated state.

Fig. 1

A

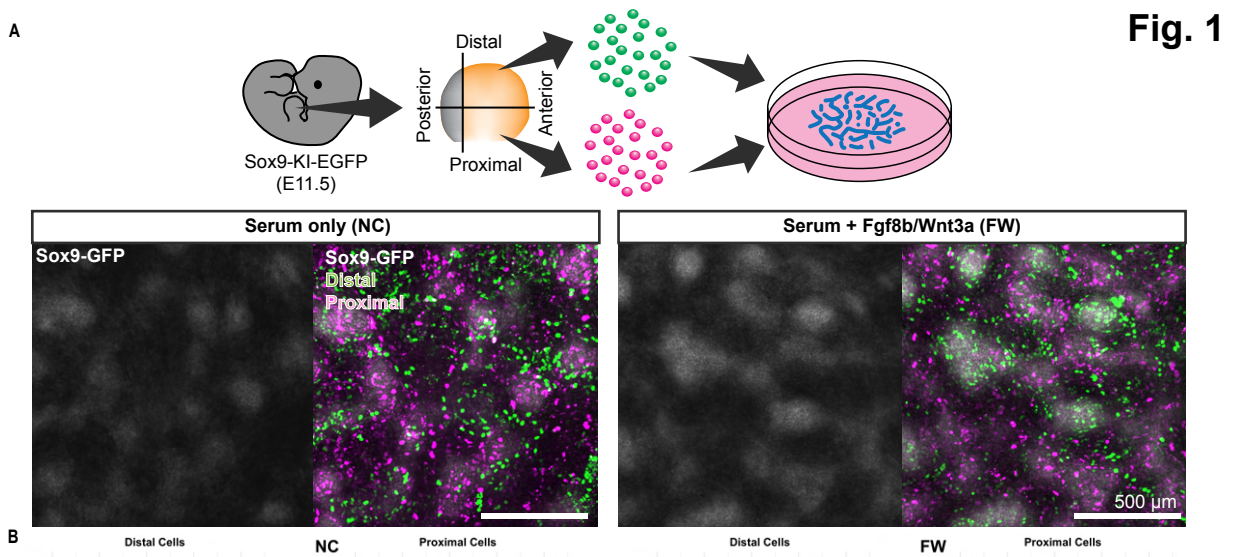

B

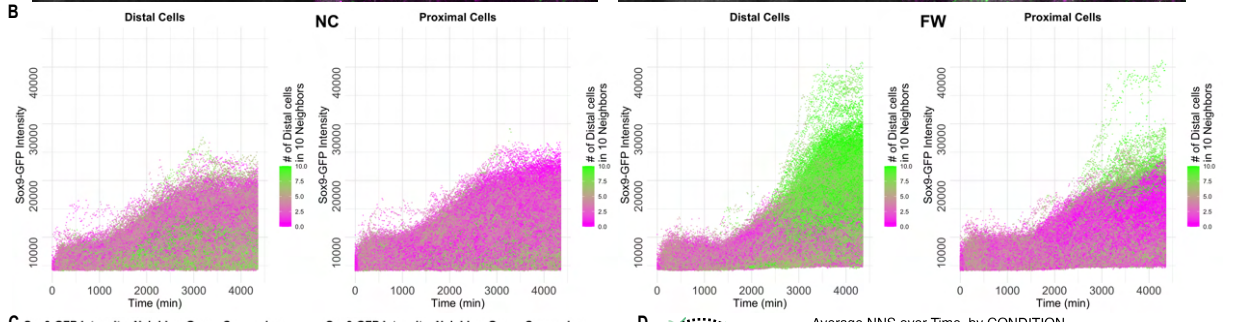

C

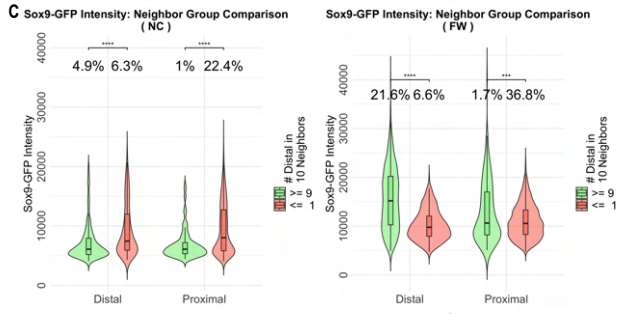

D

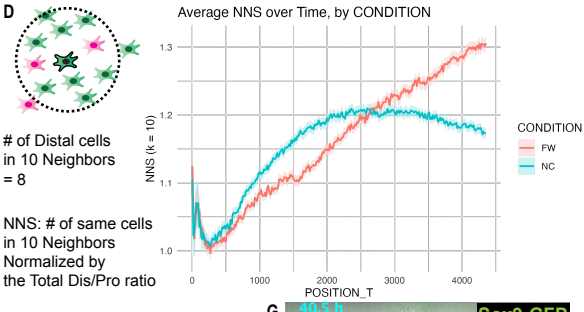

E

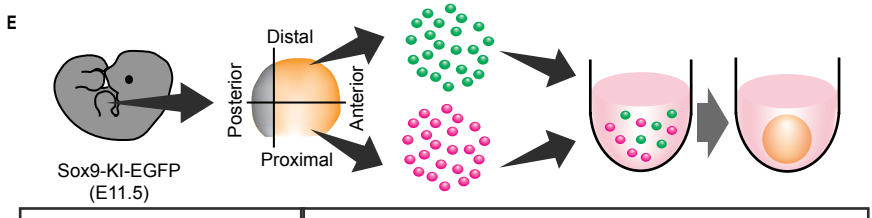

F

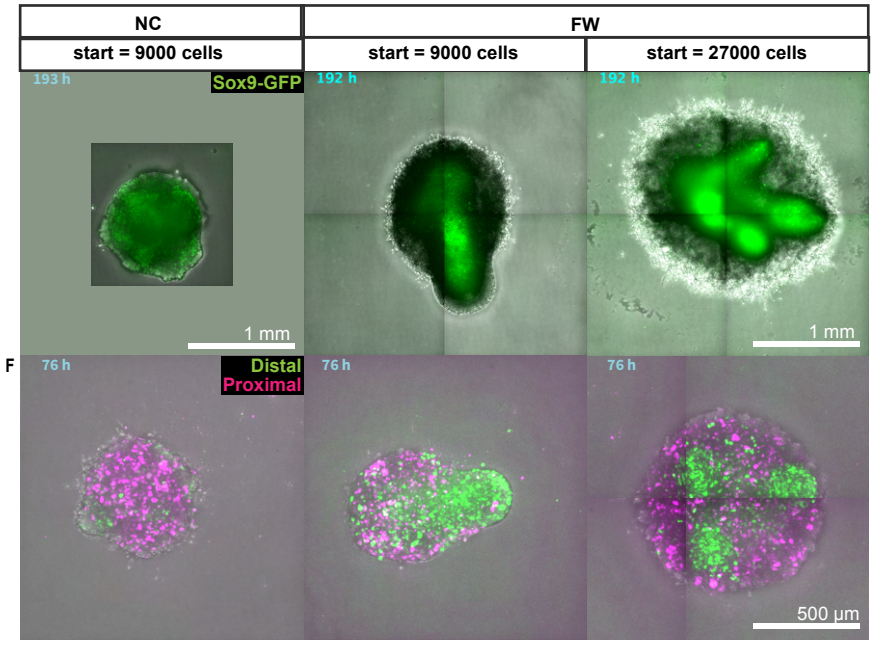

G

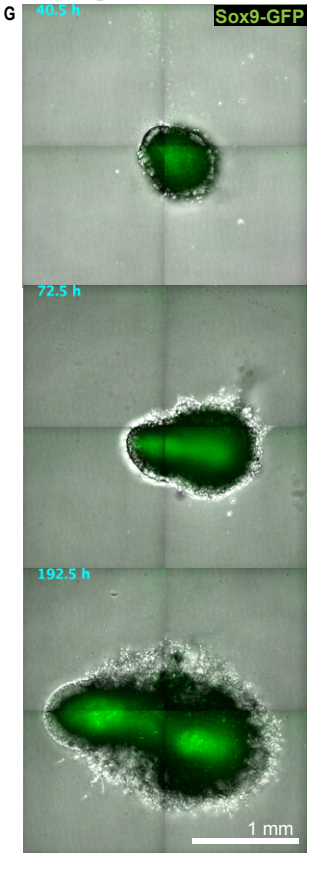

Fig. S1

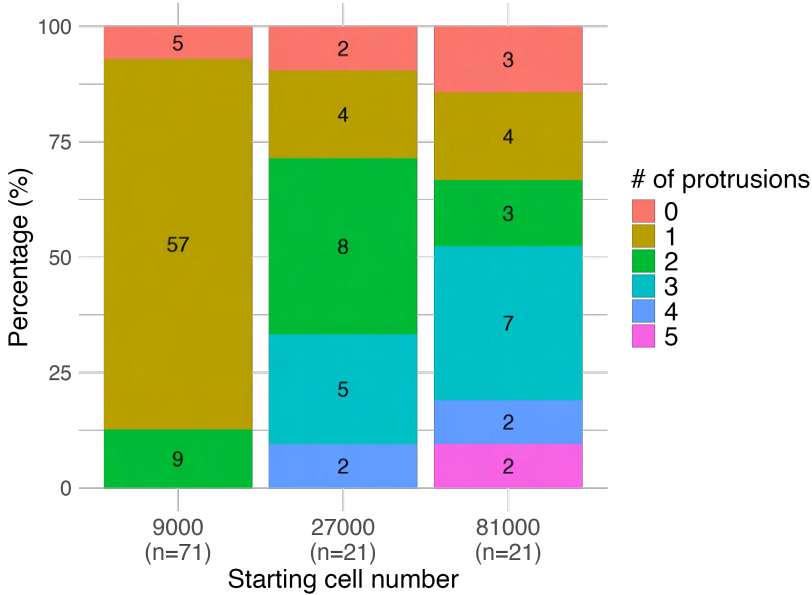
100
75
50
25
0
Percentage (%)
5
57
9
2
4
8
5
2
3
4
3
7
2
2
9000
(n=71)
27000
(n=21)
81000
(n=21)
Starting cell number
# of protrusions
0
1
2
3
4
5

Fig. S2

A

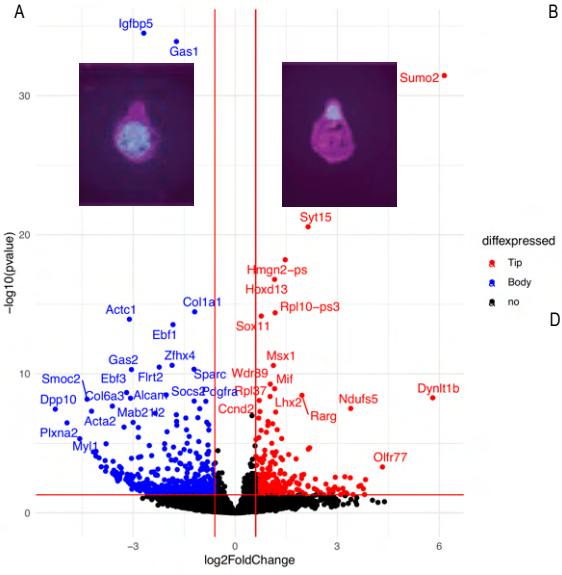

B

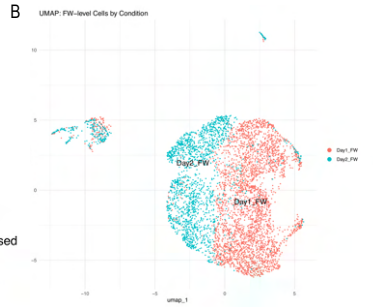

C

Marker detection (≥1 UMI per gene)

Gene	% cells detected	Tissue
Epcam	8.26	Surface ectoderm
Cdh1	4.85	Surface ectoderm
Wnt6	1.24	Surface ectoderm
Krt8	1.02	Surface ectoderm
Krt18	8.70	Surface ectoderm
(≥2 genes, ≥1 UMIs)	2.64	Surface ectoderm
Fgf8	1.46	AER
Wnt3a	0.536	AER
Krt5	0	AER
Krt14	0.0575	AER
Trp63	2.93	AER
(≥2 genes, ≥1 UMIs)	0.172	AER
Prrx1	95.2	Limb mesenchyme
Hand2	56.5	Limb mesenchyme
Tbx5	58.4	Limb mesenchyme
Pdgfra	64.6	Limb mesenchyme
Hoxa13	59.5	Limb mesenchyme
(≥2 genes, ≥1 UMIs)	91.0	Limb mesenchyme

D

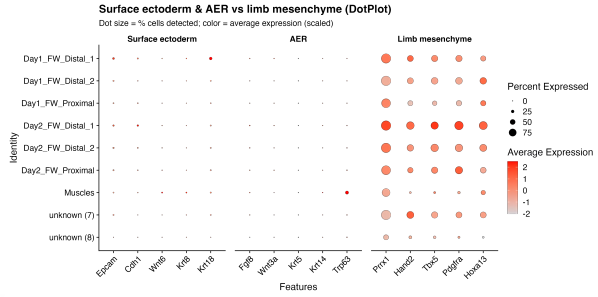

E

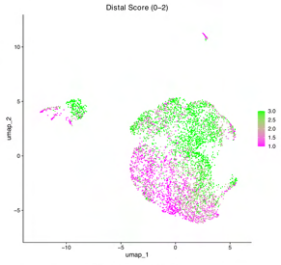

F

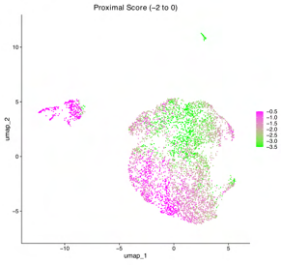

G

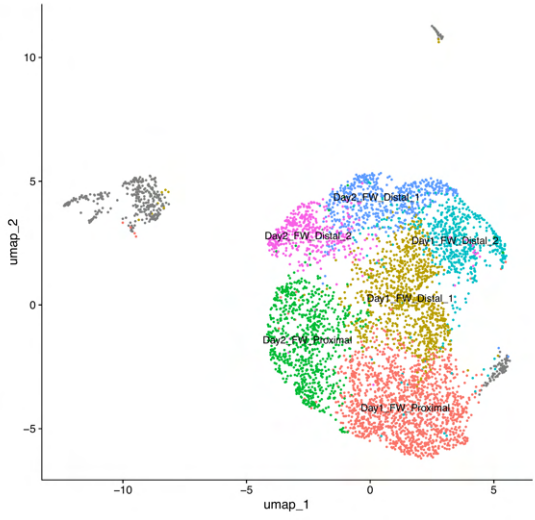

H

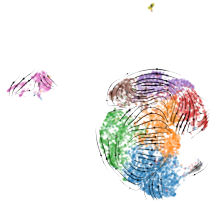

I

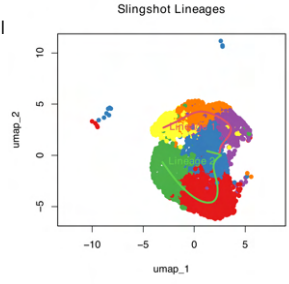

J

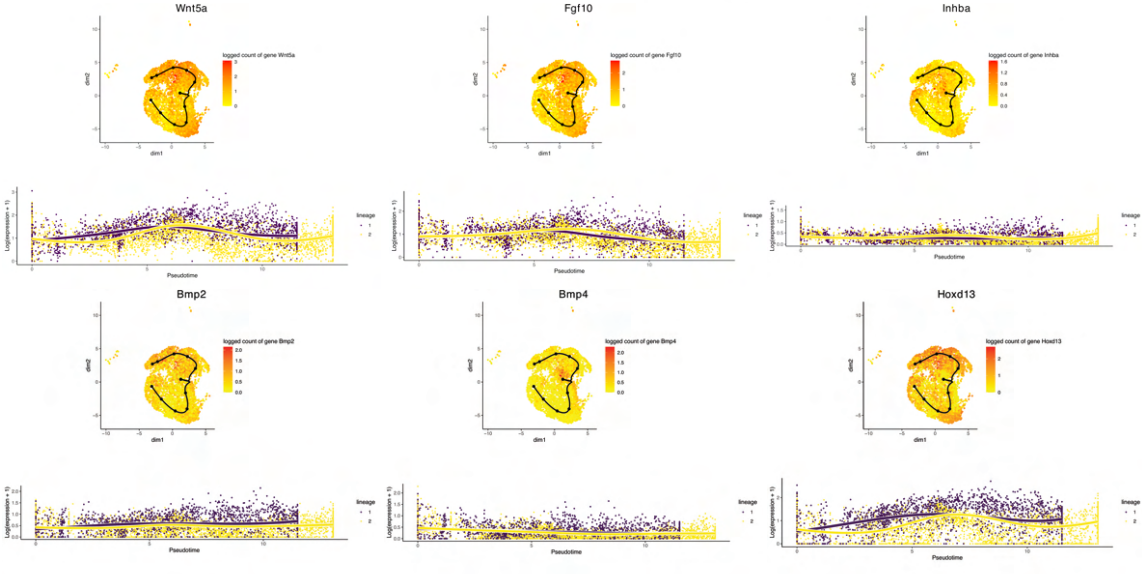

Fig. S3

A

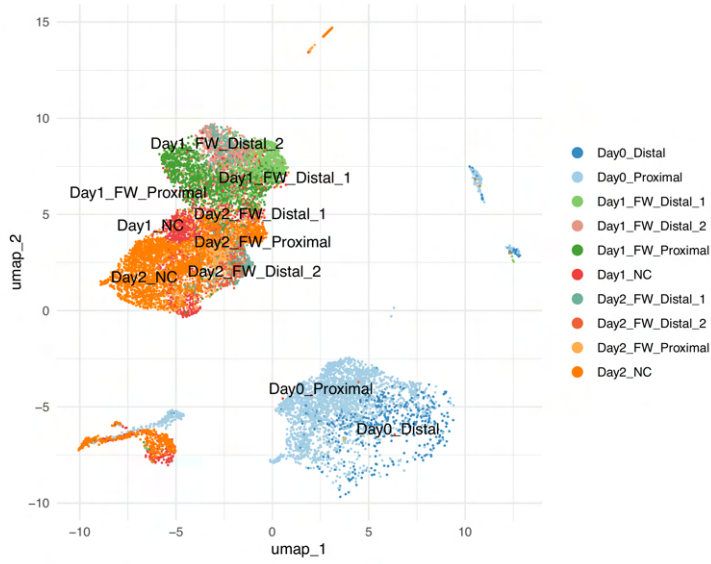

B

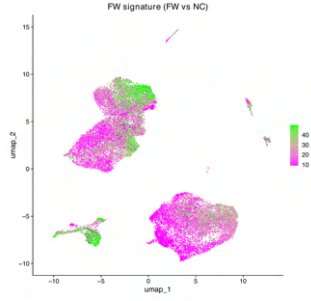

C

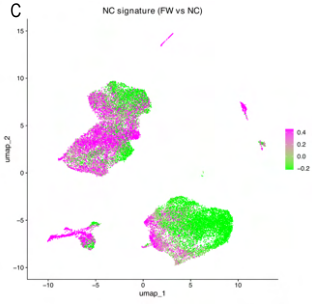

D

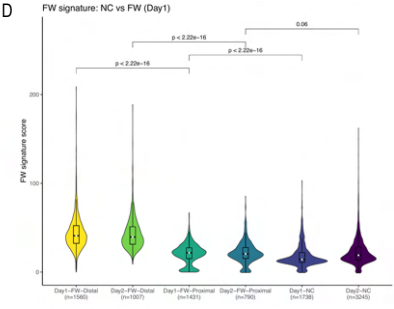

E

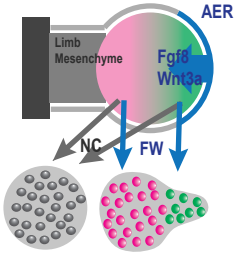

F

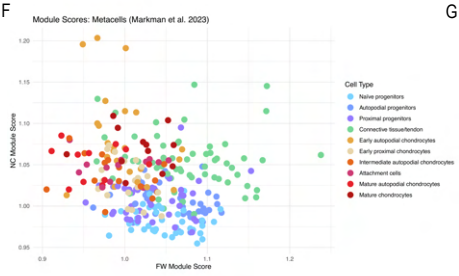

G

Fig. 2

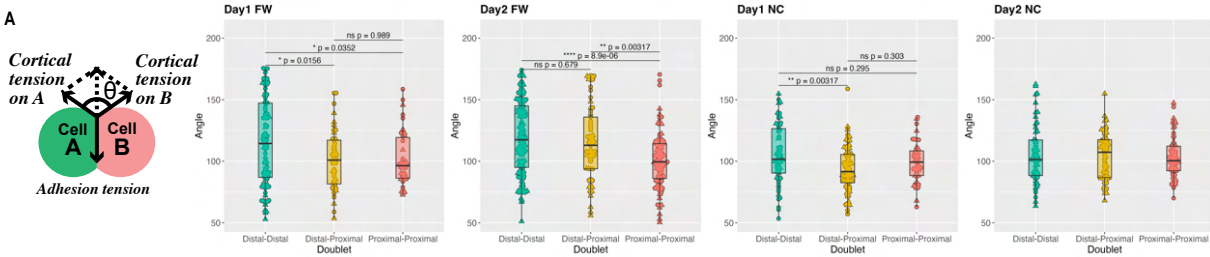
A
Cortical tension on A
Cortical tension on B
θ
Cell A
Cell B
Adhesion tension
Day1 FW
Day2 FW
Day1 NC
Day2 NC
Angle
Doublet
Distal-Distal
Distal-Proximal
Proximal-Proximal
ns p = 0.989
* p = 0.0352
* p = 0.0156
ns p = 0.679
**** p = 8.9e-06
** p = 0.00317
ns p = 0.303
ns p = 0.295
** p = 0.00317

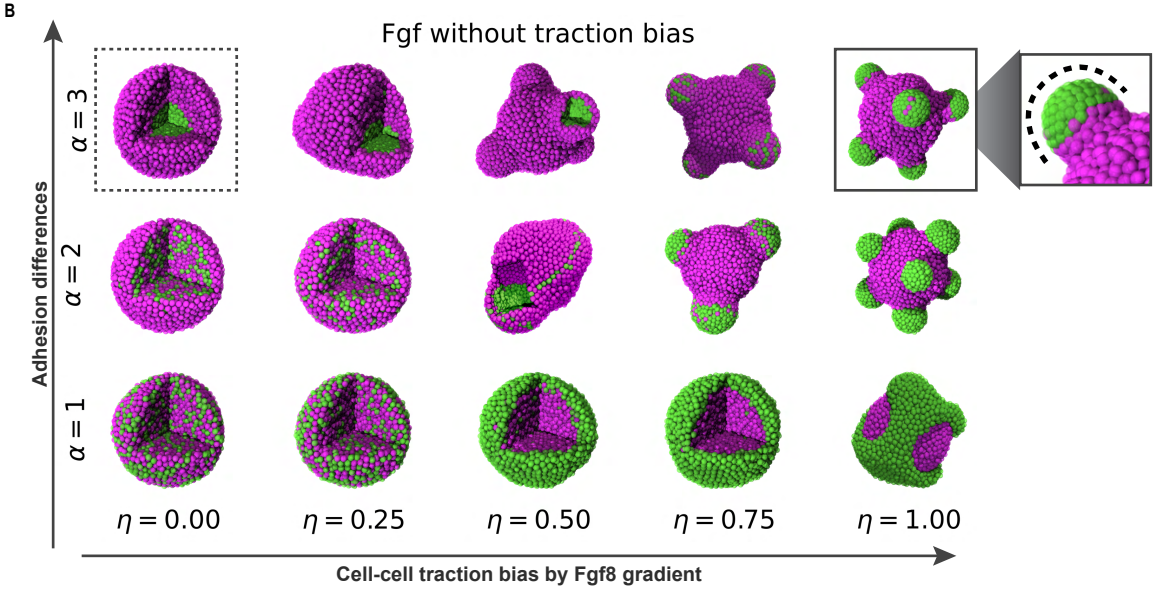
B
Fgf without traction bias
Adhesion differences
α = 3
α = 2
α = 1
η = 0.00
η = 0.25
η = 0.50
η = 0.75
η = 1.00
Cell-cell traction bias by Fgf8 gradient

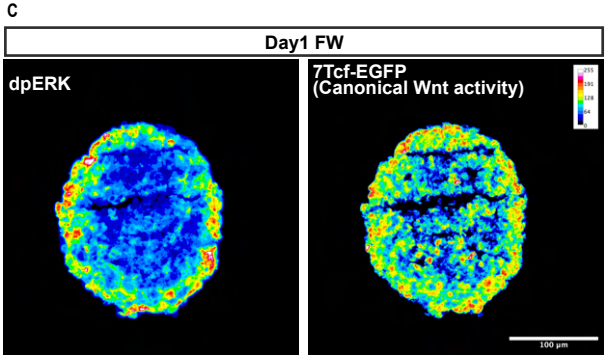
C
Day1 FW
dpERK
7Tcf-EGFP
(Canonical Wnt activity)
100 µm

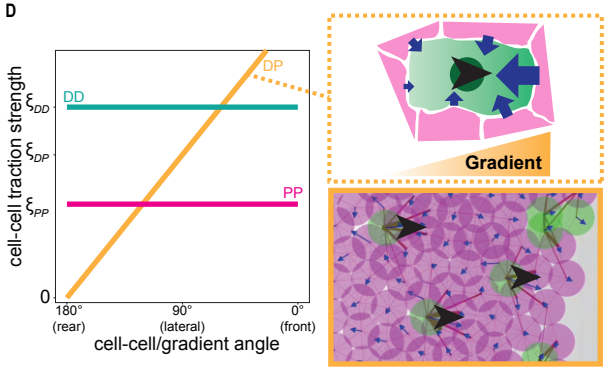
D
cell-cell traction strength
DD
DP
PP
ξ_{DD}
ξ_{DP}
ξ_{PP}
0
180°
(rear)
90°
(lateral)
0°
(front)
cell-cell/gradient angle
Gradient

Fig. S4

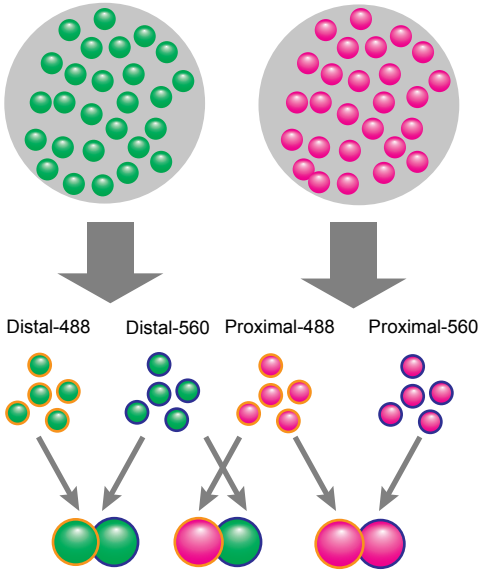

Fig. 3

A

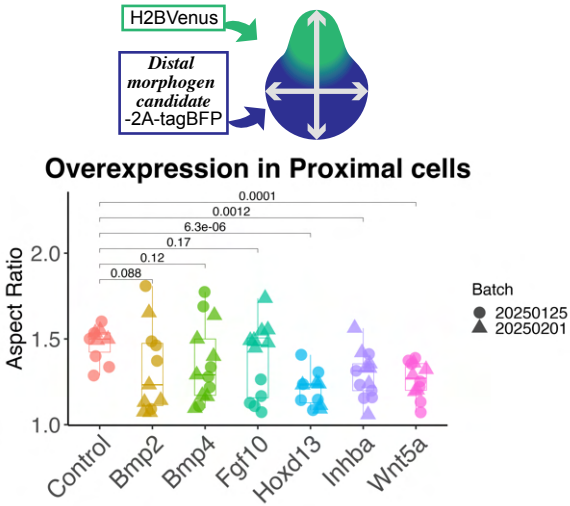
H2BVenus
Distal morphogen candidate -2A-tagBFP
Overexpression in Proximal cells
Aspect Ratio
0.0001
0.0012
6.3e-06
0.17
0.12
0.088
Control
Bmp2
Bmp4
Fgf10
Hoxd13
Inhba
Wnt5a
Batch
20250125
20250201

B

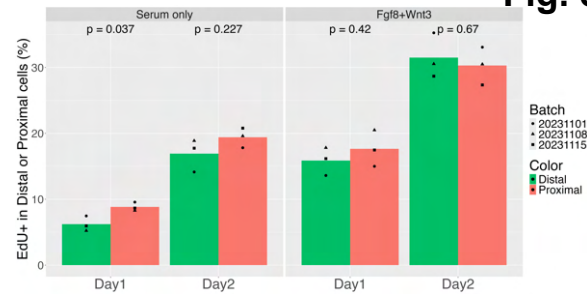
Serum only
Fgf8+Wnt3
p = 0.037
p = 0.227
p = 0.42
p = 0.67
EdU+ in Distal or Proximal cells (%)
Day1
Day2
Batch
20231101
20231108
20231115
Color
Distal
Proximal

C

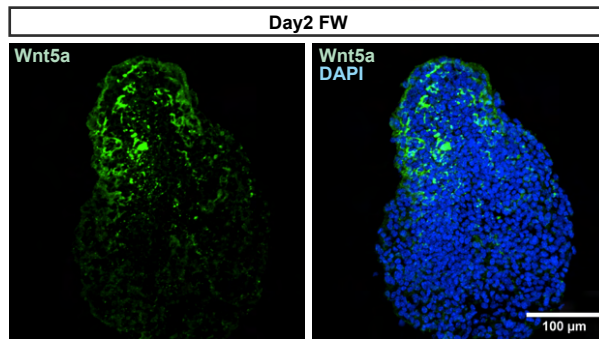
Day2 FW
Wnt5a
Wnt5a
DAPI
100 µm

D

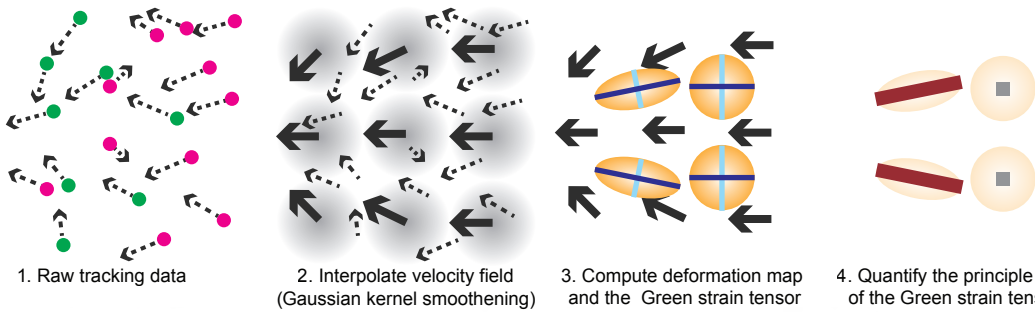
1. Raw tracking data
2. Interpolate velocity field (Gaussian kernel smoothening)
3. Compute deformation map and the Green strain tensor
4. Quantify the principle axis of the Green strain tensor

E

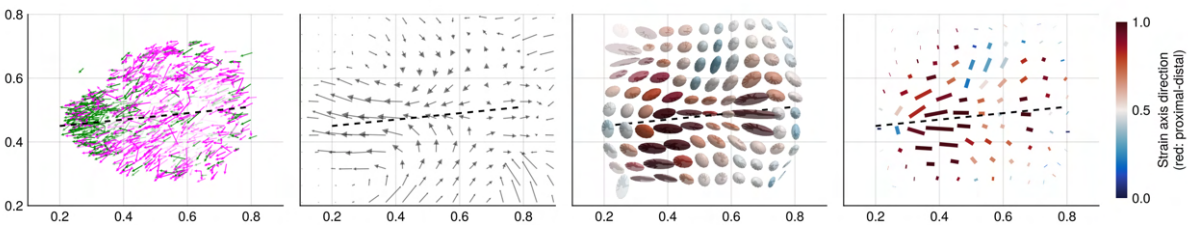
2D Slice (frame 30)
Continuous Vectorfield
Cauchy-Green Strain Tensor
Convergent-Extension Axes (CE)
Strain axis direction (red: proximal-distal)

F

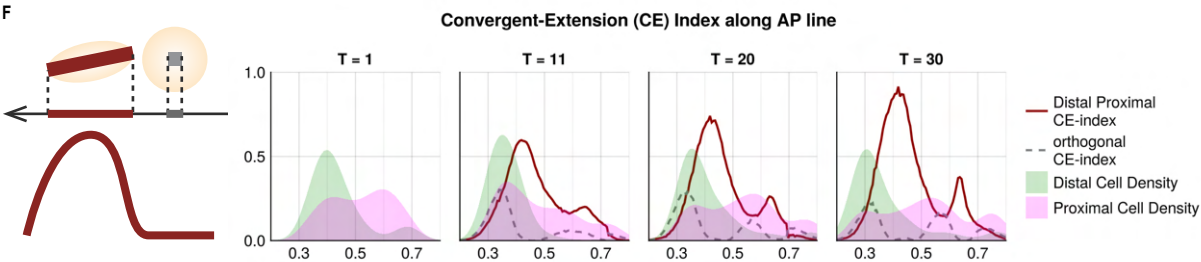
Convergent-Extension (CE) Index along AP line
T = 1
T = 11
T = 20
T = 30
Distal Proximal CE-index
orthogonal CE-index
Distal Cell Density
Proximal Cell Density

Fig. S5

A

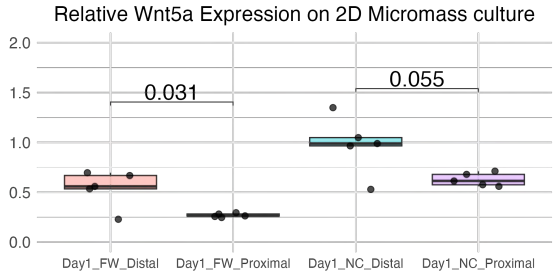
Relative Wnt5a Expression on 2D Micromass culture
2.0
1.5
1.0
0.5
0.0
0.031
0.055
Day1_FW_Distal
Day1_FW_Proximal
Day1_NC_Distal
Day1_NC_Proximal

Fig. 4

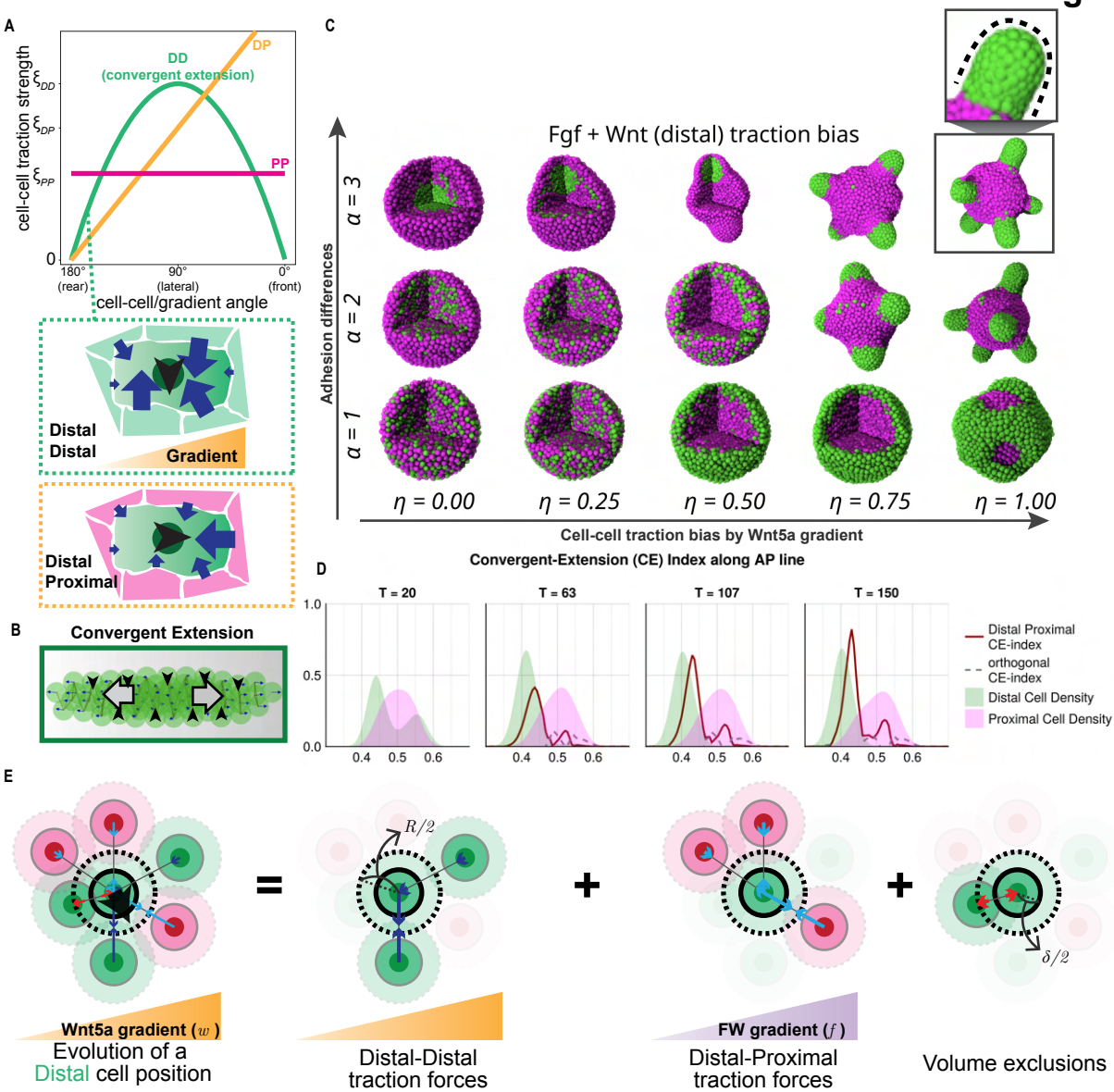

F Evolution of a Distal cell position

$$\dot{x}_i^D = \frac{1}{N}\sum_{j\in D}\xi_{DD}\big(1+\eta_D^{DD}\langle\hat{z},w\rangle\big)\big(1-\eta_D^{DD}\langle\hat{z},w\rangle\big)K(z)z + \frac{1}{N}\sum_{j\in P}\xi_{DP}\big(1+\eta_D^{DP}\langle\hat{z},f\rangle\big)K(z)z + \frac{1}{N}\sum_{j=1}^{N}F^{\text{rep}}_{i\leftarrow j}$$

Distal-Distal traction forces — Distal-Proximal traction forces — Volume exclusions between cells within distance δ

Differential adhesion
ξ_{DD}: strong
ξ_{DP}: modest
ξ_{PP}: weak

Traction bias by Wnt5a gradient (w)
η_D^{DD}: orthogonal
η_D^{DP}: along
η_P^{PD}: none
η_P^{PP}: none

Vector between two cells within distance R

G Evolution of a Proximal cell position

$$\dot{x}_i^P = \frac{1}{N}\sum_{j\in P}\xi_{PP}K(z)z + \frac{1}{N}\sum_{j\in D}\xi_{DP}\big(1-\eta_D^{DP}\langle\hat{z},f\rangle\big)K(z)z + \frac{1}{N}\sum_{j=1}^{N}F^{\text{rep}}_{i\leftarrow j}$$

Proximal-Proximal traction forces — Proximal-Distal traction forces — Volume exclusions

H Evolution of Wnt5a concentration

$$\partial_t C_{wnt5} = -\lambda_{(wnt5)}C_{wnt5} + \mu_{(wnt5)}h_{\text{in}}(\phi_D) + D_{(wnt5)}\nabla\cdot(h_{\text{in}}(\phi_{\text{cells}})\nabla C_{wnt5})$$

Decay rate — Production by Distal cells — Diffusion inside the organoid (slow)

I Evolution of FW concentration

$$\partial_t C_{FW} = -\lambda_{(FW)}h_{\text{in}}(\phi_{\text{cells}})C_{FW} + \mu_{(FW)}h_{\text{out}}(\phi_{\text{cells}})(1-C_{FW}) + D_{(FW)}\nabla\cdot(h_{\text{out}}(\phi_{\text{cells}})\nabla C_{FW}$$

Decay rate in the organoid — Diffusion outside the organoid (saturated) — Diffusion inside the organoid (slow)

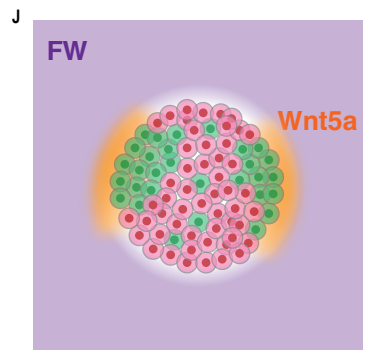

Fig. S6

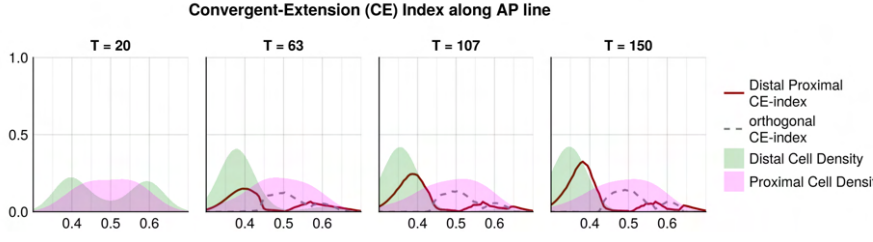
Convergent-Extension (CE) Index along AP line
T = 20
T = 63
T = 107
T = 150
1.0
0.5
0.0
0.4
0.5
0.6
Distal Proximal CE-index
orthogonal CE-index
Distal Cell Density
Proximal Cell Density

Fig. S7

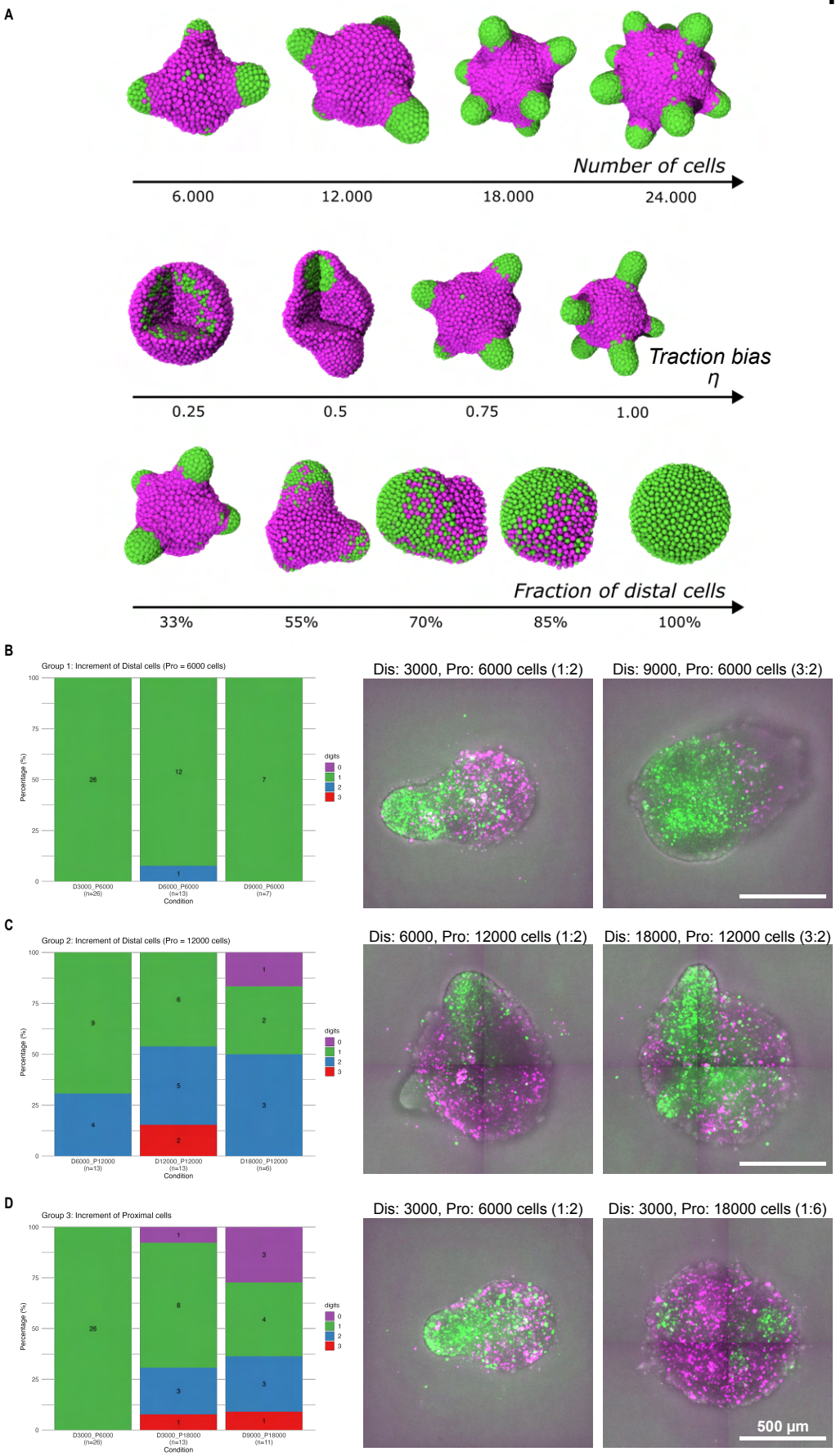
A
Number of cells
6.000
12.000
18.000
24.000
Traction bias
η
0.25
0.5
0.75
1.00
Fraction of distal cells
33%
55%
70%
85%
100%
B
Group 1: Increment of Distal cells (Pro = 6000 cells)
Percentage (%)
Condition
D3000_P6000 (n=26)
D6000_P6000 (n=13)
D9000_P6000 (n=7)
digits
Dis: 3000, Pro: 6000 cells (1:2)
Dis: 9000, Pro: 6000 cells (3:2)
C
Group 2: Increment of Distal cells (Pro = 12000 cells)
D6000_P12000 (n=13)
D12000_P12000 (n=13)
D18000_P12000 (n=6)
Dis: 6000, Pro: 12000 cells (1:2)
Dis: 18000, Pro: 12000 cells (3:2)
D
Group 3: Increment of Proximal cells
D3000_P6000 (n=26)
D3000_P18000 (n=13)
D9000_P18000 (n=11)
Dis: 3000, Pro: 6000 cells (1:2)
Dis: 3000, Pro: 18000 cells (1:6)
500 µm

Fig. 5

A

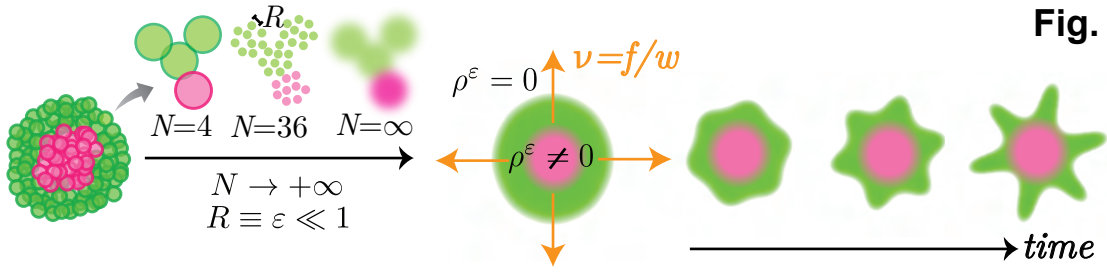

B **Evolution of Distal (x_i^D) and Proximal (x_i^P) cell positions**

$$\dot{x}_i^D = \frac{1}{N}\sum_{j\in D} F_{D\leftarrow D}(z_{ij},\nu) + \frac{1}{N}\sum_{j\in P} F_{D\leftarrow P}(z_{ij},\nu) + \frac{1}{N}\sum_{j=1}^{N} F^{\mathrm{rep}}_{i\leftarrow j}$$

$$\dot{x}_i^P = \frac{1}{N}\sum_{j\in P} F_{P\leftarrow P}(z_{ij},\nu) + \frac{1}{N}\sum_{j\in P} F_{D\leftarrow P}(z_{ij},\nu) + \frac{1}{N}\sum_{j=1}^{N} F^{\mathrm{rep}}_{i\leftarrow j}$$

C **Evolution of Distal ($\rho^{\varepsilon,D}$) and Proximal ($\rho^{\varepsilon,P}$) densities**

$$\partial_t\rho^{\varepsilon,D} = -\varepsilon^{-1}\nabla\cdot\left(\rho^{\varepsilon,D}\left(\mathcal{F}^{\varepsilon}_{D\leftarrow D}[\rho^{\varepsilon,D}] + \mathcal{F}^{\varepsilon}_{D\leftarrow P}[\rho^{\varepsilon,P}]\right)\right) + \nabla\cdot\left(\rho^{\varepsilon,D}\nabla H(\rho^{\varepsilon,D}+\rho^{\varepsilon,P})\right)$$

$$\partial_t\rho^{\varepsilon,P} = -\varepsilon^{-1}\nabla\cdot\left(\rho^{\varepsilon,P}\left(\mathcal{F}^{\varepsilon}_{P\leftarrow D}[\rho^{\varepsilon,D}] + \mathcal{F}^{\varepsilon}_{P\leftarrow P}[\rho^{\varepsilon,P}]\right)\right) + \nabla\cdot\left(\rho^{\varepsilon,P}\nabla H(\rho^{\varepsilon,D}+\rho^{\varepsilon,P})\right)$$

D

$$\boxed{\begin{aligned}\partial_t\rho_D &= -\varepsilon^{-1}\xi_{DP}\eta\nabla\cdot\left(\rho_D A^{\varepsilon}(\rho_P)\nu\right)\\ \partial_t\rho_P &= \varepsilon^{-1}\xi_{DP}\eta\nabla\cdot\left(\rho_P A^{\varepsilon}(\rho_D)\nu\right)\end{aligned}} + c_1\nabla\cdot(\rho_D\nabla q^{\varepsilon}_D) + \eta^2\xi_{DD}\nabla\cdot\left(\rho_D[c_2 D(\nu)\nabla\rho_D + \varepsilon^2\hat{R}_3(\nu,\rho)]\right)$$

$$\partial_t\rho_P = \varepsilon^{-1}\xi_{DP}\eta\nabla\cdot\left(\rho_P A^{\varepsilon}(\rho_D)\nu\right) + c_1\nabla\cdot(\rho_P\nabla q^{\varepsilon}_P)$$

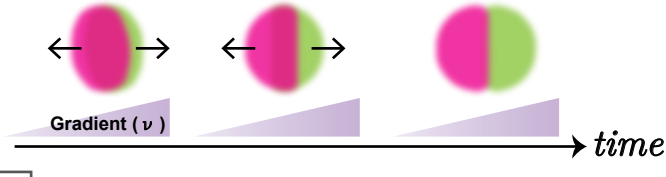

E

$$\partial_t\rho_D = \boxed{\nabla\cdot(\rho_D\nabla q^{\varepsilon})} + \varepsilon^{-1}\eta^2\nabla\cdot\left(\rho_D D(\nu)\nabla\rho_D\right), \qquad q^{\varepsilon} = \varepsilon^{-1}W'(\rho) - \varepsilon\Delta\rho$$

Cahn-Hilliard The term originated from the biased traction forces

F

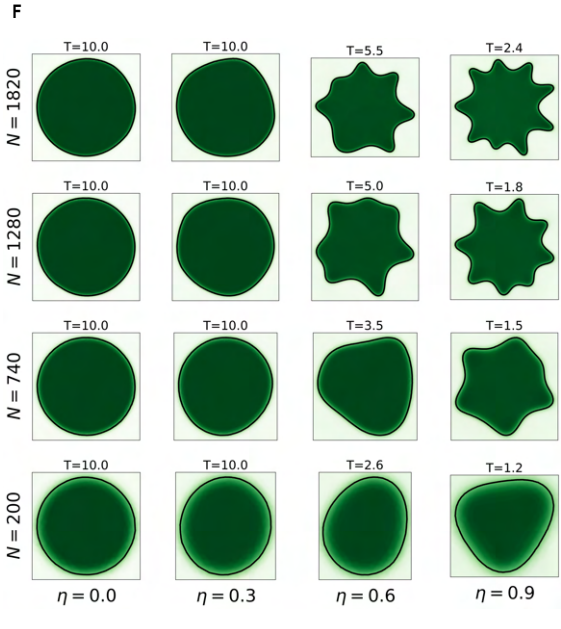

G

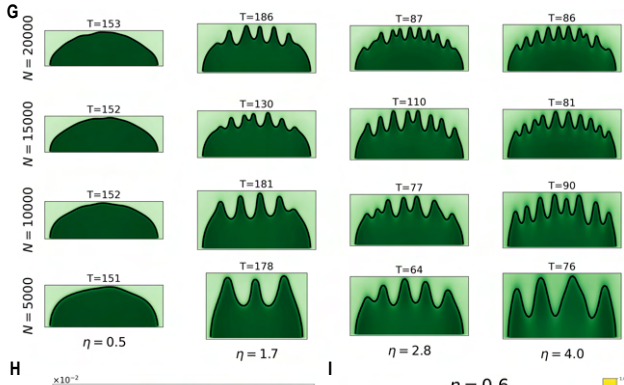

H

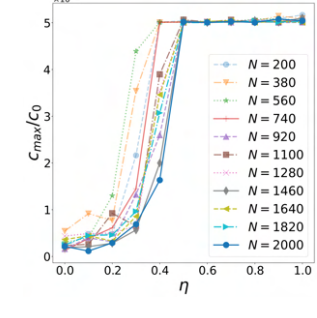
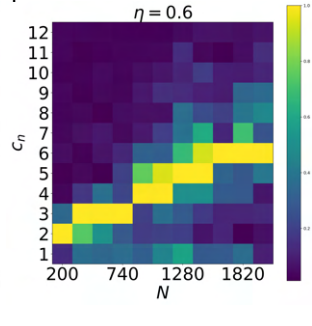
I